



Quasi-Idealized Numerical Simulations of Processes Involved in Orographic Convection Initiation over the Sierras de Córdoba

ITINDERJOT SINGH,^a STEPHEN W. NESBITT,^a AND CHRISTOPHER A. DAVIS^b

^a *University of Illinois at Urbana–Champaign, Urbana, Illinois*

^b *National Center for Atmospheric Research, Boulder, Colorado*

(Manuscript received 11 January 2021, in final form 1 December 2021)

ABSTRACT: The Sierras de Córdoba (SDC) range in Argentina is a hotspot of deep moist convection initiation (CI). Radar climatology indicates that 44% of daytime CI events that occur near the SDC in spring and summer seasons and that are not associated with the passage of a cold front or an outflow boundary involve a northerly low-level jet (LLJ), and these events tend to preferentially occur over the southeast quadrant of the main ridge of the SDC. To investigate the physical mechanisms acting to cause CI, idealized convection-permitting numerical simulations with a horizontal grid spacing of 1 km were conducted using Cloud Model 1 (CM1). The sounding used for initializing the model featured a strong northerly LLJ, with synoptic conditions resembling those in a previously postulated conceptual model of CI over the region, making it a canonical case study. Differential heating of the mountain caused by solar insolation in conjunction with the low-level northerly flow sets up a convergence line on the eastern slopes of the SDC. The southern portion of this line experiences significant reduction in convective inhibition, and CI occurs over the SDC southeast quadrant. The simulated storm soon acquires supercellular characteristics, as observed. Additional simulations with varying LLJ strength also show CI over the southeast quadrant. A simulation without background flow generated convergence over the ridgeline, with widespread CI across the entire ridgeline. A simulation with mid- and upper-tropospheric westerlies removed indicates that CI is minimally influenced by gravity waves. We conclude that the low-level jet is sufficient to focus convection initiation over the southeast quadrant of the ridge.

KEYWORDS: Cloud resolving models; Mesoscale models; Numerical weather prediction/forecasting

1. Introduction

Numerical weather prediction (NWP) models often have difficulty in accurately predicting the initiation of deep moist convection (hereafter CI). This problem is compounded in complex terrain because of additional challenges such as difficulty in faithful representation of surface layer (SL), planetary boundary layer (PBL; Rotach and Zardi 2007; Schneider and Lilly 1999; Stensrud 2007), and other terrain-related processes (e.g., Schwitalla et al. 2008), as well as challenges in obtaining observations near terrain. However, terrain is also a source of predictability: it can help constrain the area of potential CI as convergence zones are formed due to mechanisms such as thermally driven upslope flows (Banta et al. 1990; Houze 1993; Hanley et al. 2011).

CI can strongly depend upon meso- γ (2–20 km) variability in atmospheric temperature and moisture as well as land surface conditions (Weckwerth et al. 1996; Fabry 2006); terrain-impacted flows can lead to strong spatial variability in these fields which must be captured to accurately forecast CI. Forecasting of CI over terrain is crucial due to potential local severe-weather impacts and flooding, and convection often

grows upscale into mesoscale convective systems downstream of terrain.

The region encompassing the Sierras de Córdoba (SDC; Fig. 1) range in central Argentina is a prolific producer of warm-season deep moist convection. Previous studies using satellite and radar data show that thunderstorms in this region are some of the deepest convective storms in the world and produce large hail, lightning, flooding, and even tornadoes (Rasmussen and Houze 2011; Rasmussen et al. 2014; Zipser et al. 2006).

However, the flows around the SDC and role of mesoscale processes in CI are not sufficiently explored; filling these knowledge gaps could help in understanding CI processes more generally near other mesoscale terrain features. Several studies have investigated the role of synoptic-scale processes in triggering deep convection over the region downstream of the Andes and encompassing the SDC. It is hypothesized that lee-side subsidence caused by westerly flow over the Andes leads to a cap over the northerly, moist South American low-level jet (SALLJ; Vera et al. 2006; Rasmussen and Houze 2016, 2011). Various studies have shown that the SDC range acts as one of the foci of CI in the afternoon (Cancelada et al. 2020). Romatschke and Houze (2010), using data from the Tropical Rainfall Measuring Mission (TRMM) Precipitation

Corresponding author: Itinderjot Singh, isingh9@illinois.edu

DOI: 10.1175/JAS-D-21-0007.1

© 2022 American Meteorological Society. For information regarding reuse of this content and general copyright information, consult the [AMS Copyright Policy](#) (www.ametsoc.org/PUBSReuseLicenses).

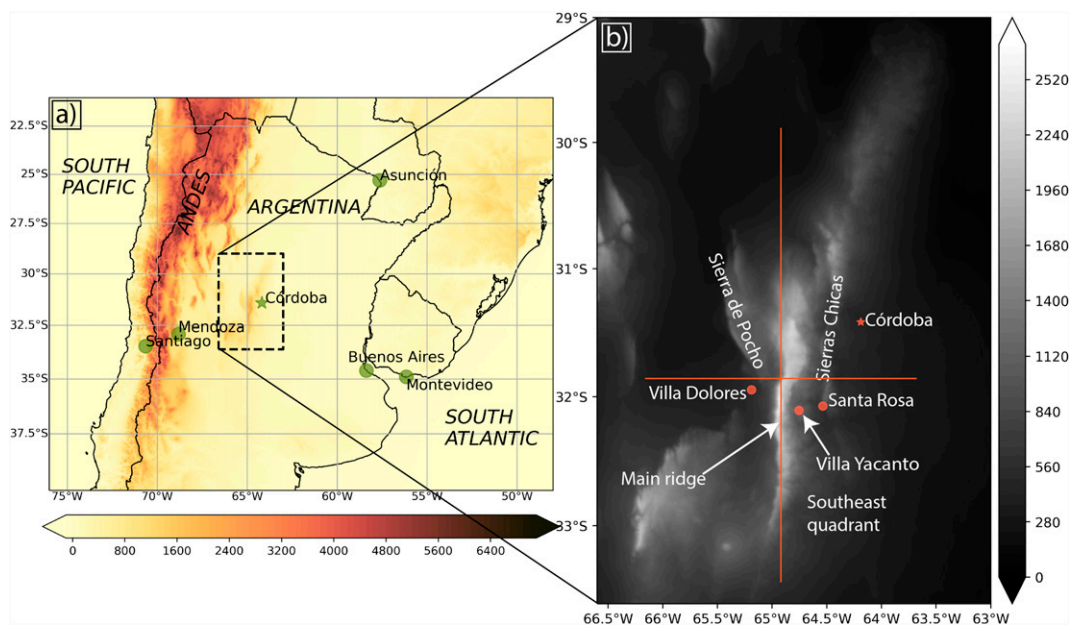


FIG. 1. (a) Terrain height (m; shaded) of a portion of the South American continent. Major cities are marked in green. The SDC region is shown enclosed in a box. (b) Terrain height (m; shaded) of the SDC region. The major north–south-oriented topographic feature is marked as “main ridge”; for ease of reference, it is divided into four quadrants, with only the southeast quadrant labeled in this figure. Two smaller mountain ranges are also labeled: Sierra de Pocho and Sierras Chicas to the west and east of the northern “head” of the main ridge, respectively.

Radar, show the presence of a warm season maximum in deep convective cores frequency over the SDC and the Andean foothills to the north. This maximum occurs during late afternoon and evening hours around 2200 UTC (1900 LT), similar to Anabor et al. (2008) and Rasmussen and Houze (2011).

Mulholland et al. (2018) used data from a C-band weather radar located in the city of Córdoba (Fig. 1) to understand the convective life cycle of storms around the SDC. Their analysis of data for two austral spring and summer seasons from 2015 through 2017 revealed a strong spatial maximum in the occurrence of CI events over the southeastern part of the main SDC ridge, centered near the city of Villa Yacanto (Fig. 1). Two temporal maxima of CI were found: a daytime maximum occurring between 1400 and 1900 UTC (1100 and 1600 LT) and a nocturnal maximum between 2300 and 0600 UTC (2000 and 0300 LT). The daytime maximum was linked to thermally driven circulations over heated terrain. Their composite, pre-convective hodographs included a veering wind profile with a northerly low-level jet (LLJ), parallel to the long axis of the SDC and centered around 800 hPa, and strong upper-level westerly flow.

While several studies have examined synoptic-scale conditions prevailing during CI, little is known regarding how the SALLJ interacts with the SDC topography to cause CI, especially in the presence of daytime upslope flows. To understand how terrain-impacted flows can lead to CI in this region, this study investigates the SDC terrain-induced modification of a typical, preconvective, daytime environment, ultimately leading to CI, using numerical simulations. This preconvective

environment consists of a northerly LLJ and strong upper-level westerly flow. This study also examines the mesoscale variation of CI events around the SDC in environments with LLJ using radar data.

There is abundant literature that deals with daytime CI over mountains. Several studies related to the Convective and Orographically Induced Precipitation field campaign (COPS; Wulfmeyer et al. 2011) highlighted the importance of low-level convergence zones over mountains, produced either by the mechanical or thermal response of the topography, or both, in causing CI over the Vosges and the Black Forest mountains (Kottmeier et al. 2008; Labbouz et al. 2013; Weckwerth et al. 2011; Corsmeier et al. 2011; Hagen et al. 2011). Hagen et al. (2011) found a strong dependence of the location of low-level convergence and CI on background wind speed and direction and the resulting Froude number.

Soderholm et al. (2014) used observations and quasi-idealized numerical simulations to investigate the evolution of thunderstorms initiating over the Black Hills (maximum height of about 2200 m) in South Dakota and Wyoming. One of the cases they analyzed shows that the presence of low-level flow parallel to the long axis of the ridge, upper-level westerlies, and daytime upslope flows leads to convergence over the ridge. Eventually, when storms initiate over this line and then mature, the outflow from the storms moves downwind (with respect to the low-level flow) and does not disrupt the upslope flow, leading to unhindered generation of new cells. They also noted that terrain-induced changes in the vertical wind shear affect the evolution of storms downwind.

Prior work has also investigated the role of terrain in modulating severe storms. [Markowski and Dotzek \(2011\)](#), using a suite of numerical simulations with idealized terrain, found that the terrain-induced horizontal variations in CIN, relative humidity (RH), and storm-relative helicity (SRH) could strongly influence near-terrain cyclonically rotating supercells. In a related study, [Scheffknecht et al. \(2017\)](#) investigated the life cycle of a long-lived supercell that initiated ahead of a cold front over complex topography along the main Alpine ridge in Switzerland and Austria. They found that regional-scale thermal circulations helped enhance the vertical wind shear, contributing to the supercell development. They also reported that upslope circulations over smaller terrain features helped sustain the storm by moistening and deepening the PBL and reducing CIN. The modulation of PBL height and moisture, and vertical wind shear by mountain-related processes can significantly affect both initiation of shallow convection and transition of shallow to deep convection.

[Panosetti et al. \(2016\)](#) conducted large-eddy simulations (LES) and cloud-resolving model simulations (CRM) of CI caused by daytime upslope flows over two infinite ridges flanking a valley. They carried out simulations with two different mountain heights: 1) lower mountains within a stable layer and an elevated mixed layer (EML) above and 2) higher mountains penetrating the EML. They found that in case of lower mountains, the presence of cross-barrier background winds weakens the updrafts and causes CI to occur downwind of the ridgetop. But in case of higher mountains, it strengthens the updrafts. Stronger ambient winds lead to downwind shifting of the convective cores, leading to stronger upslope flow and stronger upslope moisture advection over the lee of the mountains and causing increased precipitation over the downwind lee.

It is quite clear that topography asserts a significant influence on the surrounding kinematic and thermodynamic environment, playing important roles in the timing and location of CI. The objective of this study is to investigate the mesoscale dynamics of daytime CI over the SDC during a commonly observed preconvective environment. The science questions addressed in this paper are as follows: 1) Are there any preferred regions for CI in observations? 2) How does the background flow interact with diurnally heated SDC terrain in the numerical simulations? 3) How does the location of CI in the numerical simulations compare against observations for similar environmental conditions?

The simulations in this study are based on intensive observing period 4 (IOP4) of the Remote sensing of Electrification, Lightning, And Mesoscale/Microscale Processes with Adaptive Ground Observations (RELAMPAGO; [Nesbitt et al. 2021](#)) field campaign, which took place in the SDC region in November–December 2018. Data from ground-based mobile and stationary radar, radiosondes, and a host of other meteorological instruments were collected to understand the evolution of storms in this region. The IOP4 environment, discussed in detail in [section 3b](#), is similar to the canonical, preconvective environment around the SDC as described in [Rasmussen and Houze \(2016\)](#). The IOP4 preconvective hodograph used in this study also resembles the ERA-Interim-

derived composite hodographs presented in [Mulholland et al. \(2018\)](#). A suite of quasi-idealized numerical modeling experiments using isolated SDC topography and an initial sounding based on an observed IOP4 sounding is conducted as part of this study to explain the climatological distribution of CI around the SDC for similar preconvective environments rather than specifically explaining the events that occurred during IOP4. Nevertheless, limited comparisons are drawn between the model results and IOP4 observations in order to gain confidence in the ability of the model to simulate real events.

2. CI climatology

[Mulholland et al. \(2018\)](#) compiled a list of 113 CI events that took place near the SDC during two austral spring and summer seasons from 2015 to 2017 using data from a C-band radar located in the city of Córdoba, categorizing events based on storm morphology. They defined a CI event as the first appearance of a 30-dBZ echo over a minimum of five radar gates at the 0.5° scan angle. To determine if the CI events related to diurnal mountain heating occur over a preferential location, all the events in the above-mentioned list that occur between 1100 and 2000 UTC (0800 and 1700 LT) and do not appear to be related to the passage of a front or an outflow boundary of distant convection were chosen. We identified 41 such events; they all occurred in close proximity to the SDC terrain ([Fig. 2a](#)).

Next, preconvective, upstream (with respect to the low-level northerly flow) hodographs were generated for these 41 events by averaging the wind fields from ERA5 reanalysis ([Bell et al. 2020](#); [Hersbach et al. 2019](#)) over an area of 1° × 1° centered at 28.5°S, 63.5°W, which is north of the SDC. Hodographs whose meridional wind field contain a local maximum of at least 8 kt (1 kt ≈ 0.51 m s⁻¹) between 900 and 700 hPa were said to contain an LLJ. Based on manual inspection of hodographs, it was determined that out of these 41 daytime CI events, 18 (44%) had a northerly LLJ ([Fig. 2b](#)). Note that this statistic does not necessarily imply that LLJ is the major driver of the CI here. However, there is enough evidence in literature that points to the LLJ being associated with deep moist convection in the region ([Rasmussen and Houze 2016](#); [Piersante et al. 2021](#)). For the subset of cases when an LLJ is present, the CI field is meridionally elongated and is more tightly confined to eastern slopes of the main ridge of the SDC unlike in [Fig. 2a](#). Another noteworthy difference appears between LLJ and non-LLJ cases. The four CI events that occur on the northern tip of the main ridge of the SDC ([Fig. 2a](#)) are associated with non-LLJ environments; they do not appear in [Fig. 2b](#). This is interesting as one would intuitively expect a strong northerly flow within an LLJ to potentially lead to CI in this area due to orographic ascent. With regards to storm morphology, out of the 18 daytime CI events that are associated with an LLJ event, 7 (39%) led to the

¹ Most LLJ maxima were stronger than this; note that the wind fields are averaged over a 1° × 1° region.

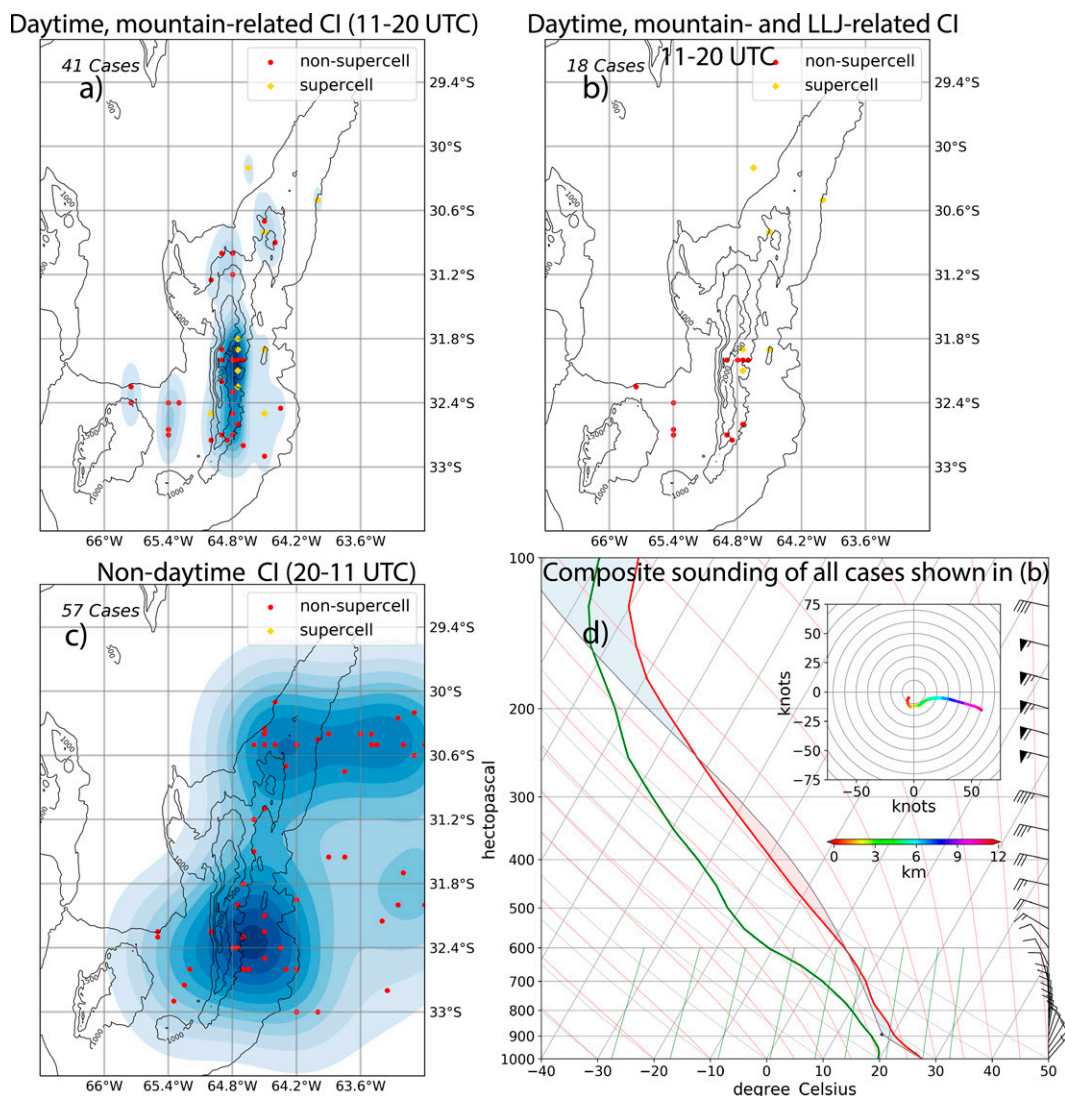


FIG. 2. Locations and kernel density estimation (blue shading; Scott 2015) of CI events occurring between (a) 1100 and 2000 UTC (41 events), (b) 1100 and 2000 UTC and having an LLJ (18 events), (c) 2000 and 1100 UTC (57 events), and (d) area-averaged composite sounding and hodograph for the events shown in (b). For the barbs in (d), a half barb = 5 kt, a full barb = 10 kt, and a pennant = 50 kt.

formation of at least one supercell. Out of the 23 non-LLJ, daytime CI events, 7 (30%) led to the formation of at least one supercell. The CI density field of all non-daytime cases is also presented (Fig. 2c), showing that CI in these cases happens near and apart from the terrain. Given these results, this study will try to present plausible hypotheses for the observed differences between the daytime CI density field for LLJ and non-LLJ environments in the context of the results from numerical simulations presented later in the paper. The area-averaged (over an area of $1^\circ \times 1^\circ$ centered at 28.5°S , 63.5°W), preconvective, composite hodograph (Fig. 2d) for all daytime-LLJ CI events shows surface northeasterlies, a local maximum of 12 kt in northerly wind around 2 km MSL, and upper-level northwesterlies with a magnitude of 60 kt around 200 hPa.

3. Model setup

Cloud Model 1 (Bryan and Fritsch 2002; version 19.8) was used for numerical simulations. The model domain has an area of $1080 \text{ km} \times 1080 \text{ km}$. The horizontal grid spacing is 1 km in both directions. While 1-km horizontal grid spacing is not sufficient to resolve PBL-scale processes, it should be able to simulate the mesoscale flow around the SDC and the thermally driven upslope flows. The model uses a terrain-following vertical coordinate system with the top located 26 km AGL. The vertical grid spacing is 100 m between the ground and 5000 m AGL; it then linearly increases to 400 m at 10000 m AGL and thereafter remains constant at that value up to the model top. The boundary conditions are open-radiative lateral boundaries, a semislip lower boundary, and a free-slip upper

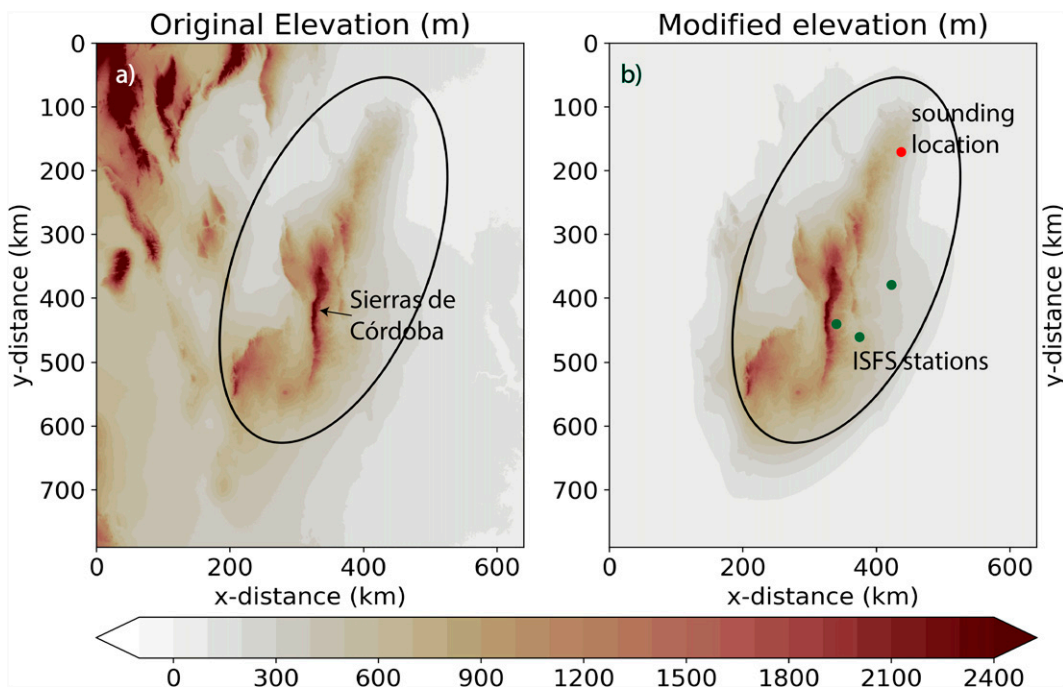


FIG. 3. (a) Actual terrain height (m; shaded) of the region; (b) terrain height (m; shaded) used in the model (before smoothing and addition of flat padding on the sides). The plot in (b) is obtained when the terrain of (a) inside the ellipse is retained as it is, while that outside the ellipse decays exponentially. The sounding location is marked in red and the three ISFS stations are marked in green.

boundary. Rayleigh damping (Durrán and Klemp 1983) is used in the uppermost 10 km to absorb vertically propagating gravity waves. The Coriolis parameter is set to $-0.771 \times 10^{-4} \text{ s}^{-1}$ (for 32°S latitude). Random potential temperature perturbations of magnitude 0.1 K are added to the initial potential temperature field. An adaptive time step is used to maintain stability throughout the simulation. Based on measurements of soil temperature from three Integrated Surface Flux System (ISFS; UCAR/NCAR 1990; Sun et al. 2003) stations around the SDC (marked in green in Fig. 3b) during IOP4, the initial skin temperature of the soil is determined to be 303 K (mean of temperature data from 1100 to 1200 UTC and averaged over all three stations). The land-use category is dry cropland and pasture. The model is initialized at 1130 UTC (0830 LT) and the output is stored every 5 min until 1700 UTC (1400 LT; the CI event of interest occurs in the control simulation around 1710 UTC); after 1700 UTC, the output is stored every minute to capture the growth of updrafts with high temporal resolution. The simulation ends at 2200 UTC (1900 LT) on the same day. The model physics and other parameters are described in Table 1.

a. Model terrain

The model terrain is derived from the actual terrain of the SDC region. High-resolution Shuttle Radar Topography Mission (SRTM; JPL 2014; Farr et al. 2007) data are resampled to the model grid spacing of 1 km. Figure 3a shows the regional topography with an ellipse around the SDC; the minor and major axes of the ellipse are 290 and 600 km long, respectively. The terrain inside the ellipse is kept as it is while

the terrain outside the ellipse, including the Andean topography to the west, decays exponentially (Fig. 3b). Finally, the topography is smoothed using a Gaussian filter (Virtanen et al. 2020) before providing as input to the model.

Isolating the SDC terrain in an idealized model framework allows us to focus on the local terrain-related mesoscale dynamics of CI in the region while neglecting the active role of the Andes and the associated large-scale processes. It must be noted that the initial thermodynamic profile used in the model (discussed in section 3b) is influenced by processes related to the Andean terrain and synoptic-scale dynamics, e.g., the presence of an elevated mixed layer (EML; Ribeiro

TABLE 1. Description and references of model physics.

Model characteristic/ parameter	Reference/value
PBL	Yonsei University (YSU; Hong et al. 2006)
Scalar advection	Weighted essentially nonoscillatory (WENO) advection (Kang et al. 2011)
SGS turbulence	Smagorinsky scheme (e.g., Stevens et al. 1999)
Radiation	NASA Goddard scheme
Surface layer	Modified version of WRF similarity theory surface-layer scheme (Jiménez et al. 2012)
Microphysics	Morrison double-moment scheme (Morrison et al. 2009)

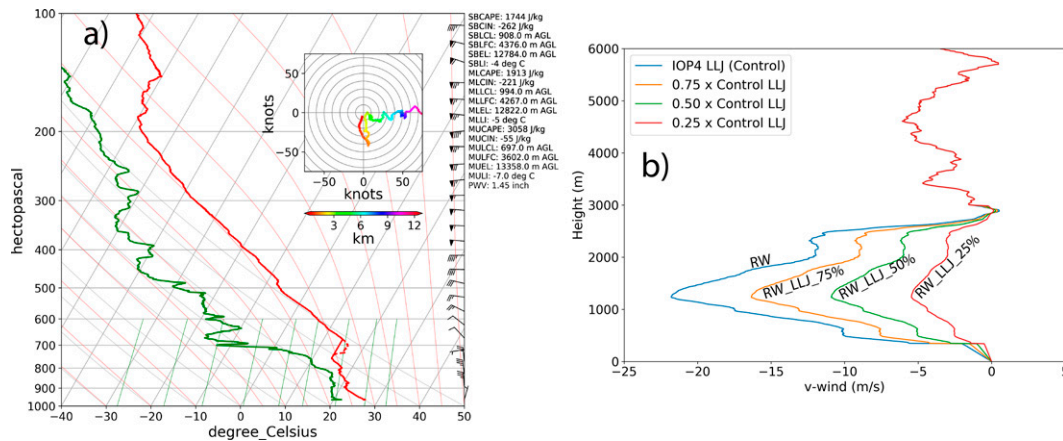


FIG. 4. (a) Sounding used to initialize the model. This sounding was taken at 1130 UTC at Villa María del Río Seco (Fig. 3b) during IOP4 of RELAMPAGO. The dashed portion of the red line is the original temperature. The solid line in that layer represents the modified temperature; this modified profile was used in the model. For the barbs, a half barb = 5 kt, a full barb = 10 kt, and a pennant = 50 kt. Several thermodynamic and kinematic variables/indices deduced from the modified sounding are also listed. (b) Variation of meridional wind (m s^{-1}) with height (MSL; m) for different LLJ strength modification experiments.

and Bosart 2018) and the SALLJ. This approach saves computational resources and is similar to the one used in Soderholm et al. (2014), who isolated the topography of the Black Hills mountain in South Dakota and Wyoming while analyzing the evolution of storms initiating over the mountain.

b. Initial sounding

The initial model environment is based on an observed 1130 UTC sounding taken on 10 November 2018 at Villa María del Río Seco (VMDRS), located upstream of the main ridge of the SDC (red dot in Fig. 3b), during IOP4 of the RELAMPAGO field campaign (UCAR/NCAR 2020). This sounding was chosen for several reasons. First, we wanted to use a sounding from a real case rather than from reanalysis data as the latter are smoothed out in the vertical and do not contain well-defined inversion layers. These layers suppress widespread convection and allow CAPE to get to very high values, consequently, producing intense convection in localized regions. The IOP4 sounding taken at VMDRS is a relatively “clean” LLJ sounding with no conspicuous adulteration due to local terrain features and preexisting convection; unfortunately, soundings were launched rather infrequently at VMDRS during RELAMPAGO. Other locations with higher radiosonde launch frequency such as Córdoba city lie further downstream (with respect to the low-level flow) and their wind fields may be affected by topographic features such as the northern Sierras Chicas.

The IOP4 sounding used in this study has a dry adiabatic mixed layer from the surface to 900 hPa and an EML from 700 to 500 hPa, with a strong capping inversion at the base of the EML (Fig. 4a). The background wind profile consists of northerly low-level flow with a local maximum of 40 kt around 850 hPa (indicative of the SALLJ), veering winds with height, and upper-level westerlies. Compared to the magnitudes of the LLJs in cases described in section 2, the IOP4

LLJ is particularly strong. The synoptic conditions during this event comprised of an upper-level trough just west of the Andes, with a closed circulation at 500 hPa and a strong westerly upper-level jet over the region (not shown). This trough provided synoptic–dynamic lift in the region and led to the formation of a lee-side low, east of the Andes and centered to the north of the SDC, which strengthened the SALLJ. A detailed description of IOP4 synoptic conditions can be obtained from the RELAMPAGO field catalog (<http://catalog.eol.ucar.edu/relampago>).

The mesoscale situation during the event, however, was quite complex and involved a series of storms generated by the cold pools of previous storms. Ultimately, a supercell formed near Santa Rosa (Fig. 1) around 1900 UTC and moved eastward [see Trapp et al. (2020) for a detailed observational analysis of this event]. Since the scope of this study is limited to investigating the interactions between a commonly occurring preconvective environment and heated SDC terrain in an idealized setting, the cold pools generated by previous storms as observed during IOP4 are not simulated. Thus, CI in the numerical simulations in this study is different from that observed during IOP4 in terms of the mechanisms involved, timing, and location. However, the model is still expected to provide a reasonably faithful simulation of the pre-CI, real mesoscale flow around the mountain. It is important to note that in the present study, CI is defined “retrospectively” as the appearance of 35-dBZ model simulated reflectivity echoes (at the lowest model level) which eventually become deep convective cores, i.e., 35-dBZ echoes which remain shallow are not considered CI. Convective cells are defined as areas of upward motion that show at least 35-dBZ reflectivity values at the lowest model level. Hence, CI events are a subset of convective cells.

Using the original sounding from IOP4 did not lead to CI/deep moist convection in the simulation. In light of the

limitations of the current model setup, which ignores synoptic-scale processes such as large-scale lift and advection of heat and moisture into the lower atmosphere by the SALLJ, it was decided to compensate for these processes and initialize the model with reduced CIN. To reduce CIN, the temperature was reduced in a shallow layer centered around 700 hPa (dotted line in Fig. 4a is the original sounding), reducing SBCIN from 299 to 262 J kg⁻¹ and changing the RH in the modified layer. The simulations with and without modified soundings had nearly identical mesoscale flow around the mountain. CI occurred around 1710 UTC in the southeast quadrant of the main ridge in the simulation with reduced CIN, similar to the climatology shown in Fig. 2b.

Two groups of simulations using this modified thermodynamic profile were conducted, all with the same model setup as described in the previous section. All simulations in the first group include the diurnal cycle, i.e., time-varying incoming solar radiation (R) and surface heat and moisture fluxes as well as background flow (W). The first simulation in this group is initialized using the modified IOP4 thermodynamic profile and the observed wind field; this simulation is the control simulation and is referred to as RW (radiation and winds). Four simulations similar to RW but with different (random) perturbations added to the initial potential temperature field were also conducted to test the robustness of the results of RW (RW_ENS1, RW_ENS2, RW_ENS3, RW_ENS4). Additionally, to account for some variability in preconvective LLJ environments and in order to make our results more generalizable, we conducted three more experiments. These experiments involved the same thermodynamic profile as the control simulation (RW) but the LLJ strength is progressively decreased by 25% (Fig. 4b; essentially, the meridional flow below 3 km MSL is scaled by 0.75, 0.50, and 0.25). These three experiments are referred to as RW_LLJ_75%, RW_LLJ_50%, and RW_LLJ_25%. Finally, another simulation similar to RW is conducted except the winds above the mountain top, i.e., above 2.5 km MSL are calm (RW_2.5km_calm); this is done to test whether deep gravity waves play a role in CI.

The second group includes one simulation which has no background flow, but radiation and surface heat and moisture fluxes are on; this simulation is intended to isolate the thermal response of the mountain and is referred to as R.

4. Results and discussion

a. Mesoscale flow around the SDC: Dynamics

A calculation of Froude number ($Fr = U/Nh$, where U is the wind speed, N is the Brunt–Väisälä frequency, and h is the height of the crest; Reinecke and Durran 2008) around the sounding location, using the values $U = 15 \text{ m s}^{-1}$ (average northerly wind component between the ground and ridgetop), $N = 0.011 \text{ s}^{-1}$ (average N between the ground and ridgetop), and $h = 2000 \text{ m}$, yields $Fr = 0.68 (<1)$. This implies that initially, most of the subcrest flow is unable to ascend the ridge and instead goes around it. Indeed, Fig. 5a, which shows 10-m winds (averaged from 1530 to 1700 UTC, i.e., about 1.5 h

prior to CI; hereafter referred simply as time averaged) for the control simulation (RW), confirms that the low-level flow is being split at the northern tip of the main ridge. The blocking of the low-level, northerly flow is aided by the presence of stable layers: an inversion layer in the temperature profile, with its base around 800 hPa and an isothermal layer atop the inversion layer (Fig. 4a; both the modified and unmodified soundings contain an isothermal layer above the inversion layer). One could speculate that many preconvective environments with an LLJ have a similar cap [following the conceptual model of Rasmussen and Houze (2016)], preventing the low-level, northerly flow from ascending the northern head of the main ridge while splitting the flow into two branches. It is known that strong subsidence in the lee of the Andes is associated with lee troughing, which is conducive for a strengthened LLJ compared with cases of weak lee troughing and presumably a weaker subsidence inversion (Rasmussen and Houze 2016). This could potentially explain why the 4 CI events (out of the 41 cases of daytime, terrain-related CI discussed in section 2) that take place over the northern head of the main ridge (Fig. 2a) do not occur during LLJ days.

After splitting around the northern tip of the main ridge, the two branches (hereafter western and eastern branches) then traverse southward while curving toward the ridgeline (Fig. 5a). As the flow in the eastern branch becomes northeasterly and easterly and ascends the eastern slopes of the ridge, it collides with the northwesterly western branch coming from over the ridgetop. An 1800 UTC sounding launched at Villa Dolores (Fig. 1) on 10 November 2018 does show near-surface northwesterly flow of magnitude 2.7 kt (not shown). The collision of the two branches appears to form a convergence and deformation zone on the eastern slopes (black rectangle in Fig. 5a). While the flow around the mountain range leads to the formation of additional convergence lines in the vicinity of major topographic obstacles, this study only focuses on the convergence line on the eastern slopes of the main ridge. Figure 5 shows the position of the convergence line for all the experiments. The convergence line lies over the eastern slopes in all the experiments (with a slight eastward shift of portions of the line with increasing LLJ strength), except R (no background flow simulation), where it lies over the ridgeline. This eastward shifting may be a result of lower pressure over the east side of the main ridge relative to the west side; Fig. 6a shows time-averaged pressure perturbation, $p' = p_{\text{total}}(x, y, z, t) - p_{\text{base_state}}(z)$, for RW at model level 2 (~150 m AGL). This pressure difference across the two sides of the main ridge extends from the ground up to a little less than 3 km MSL (Fig. 6b). This west–east pressure difference is also present in RW_2.5km_calm (Fig. 6c), indicating that it can be attributed largely to the low-level flow. The three LLJ strength modification experiments also exhibit this pressure difference, with the perturbation pressure gradient across the two sides of the main ridge decreasing as LLJ strength decreases (Fig. 6d shows time-averaged p' for RW_LLJ_50%). We suspect that the interaction of the low-level northerly flow with the asymmetric terrain of the SDC leads to a wake low on the east side, helping in setting up westerly flow over the main ridge. This potential mechanism

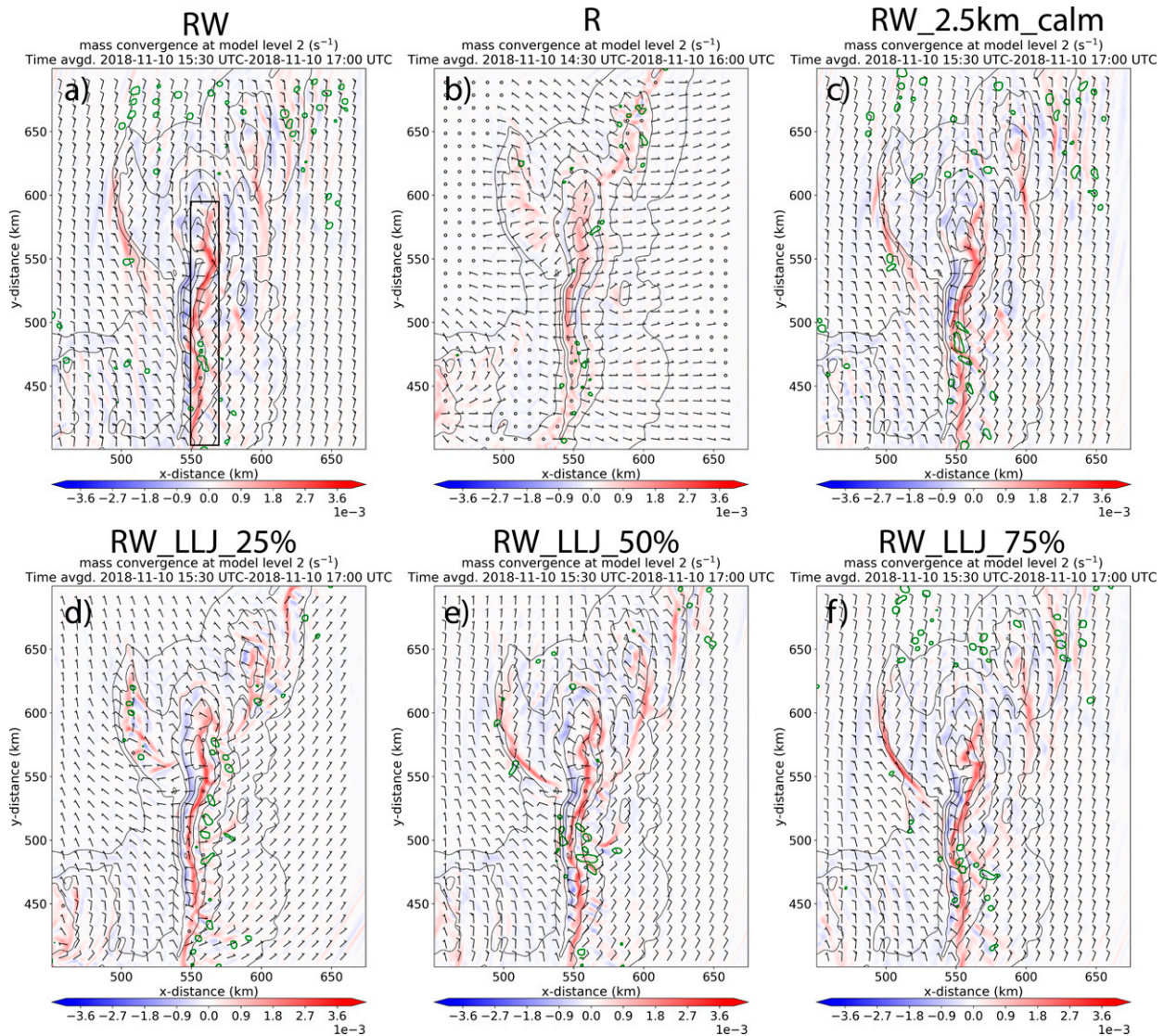


FIG. 5. Time-averaged (1530–1700 UTC) mass convergence at model level 2 (s^{-1} ; shaded contours) and 10-m wind ($m s^{-1}$; barbs) for experiments (a) RW, (b) R, (c) RW_2.5km_calm, (d) RW_LLJ_25%, (e) RW_LLJ_50%, and (f) RW_LLJ_75%. Solid green contours represent model simulated reflectivity values of 35 dBZ (at the lowest model level) at 1600 UTC for (b), and at 1700 UTC for all other panels. The black rectangle in (a) shows the convergence line of interest. For the barbs, a half barb = 5 kt, a full barb = 10 kt, and a pennant = 50 kt.

is different from that in the findings of Banta (1984, 1986), who used observations over South Park in the Colorado Rocky Mountains and 2D numerical simulations to show that convergence zones tend to develop on the lee side of the mountains (with respect to westerly flow) at the upwind edges of cold air pools in the valleys. According to Banta's studies, such a convergence zone is formed when the leeside upslope flow developing underneath the cold air converges with the flow produced due to downslope mixing of the ridgetop winds. However, in the experiments conducted in this study, it is unlikely that downward transfer of momentum contributes to the shifting of the convergence zone to the east of the ridgeline. The convergence zone appears over the eastern

slopes even in RW_2.5km_calm, where there is no flow above 2.5 km MSL and therefore, there is no downward transfer of momentum. Additionally, there is a strong synoptic inversion around 3 km MSL (Figs. 4a, 6b) that might also prevent any significant exchange of momentum.

To further understand the momentum forcings that lead to this flow configuration around the SDC, trajectory analysis was conducted. Backward trajectories for parcels present over the main ridge at model level 2 (about 150 m AGL) at 1700 UTC in RW were computed (Fig. 7). Most of these parcels originate from north of the Sierras de Córdoba (except for parcels in streams A and D). As the flow splits into two branches around the ridge head, these parcels traverse along

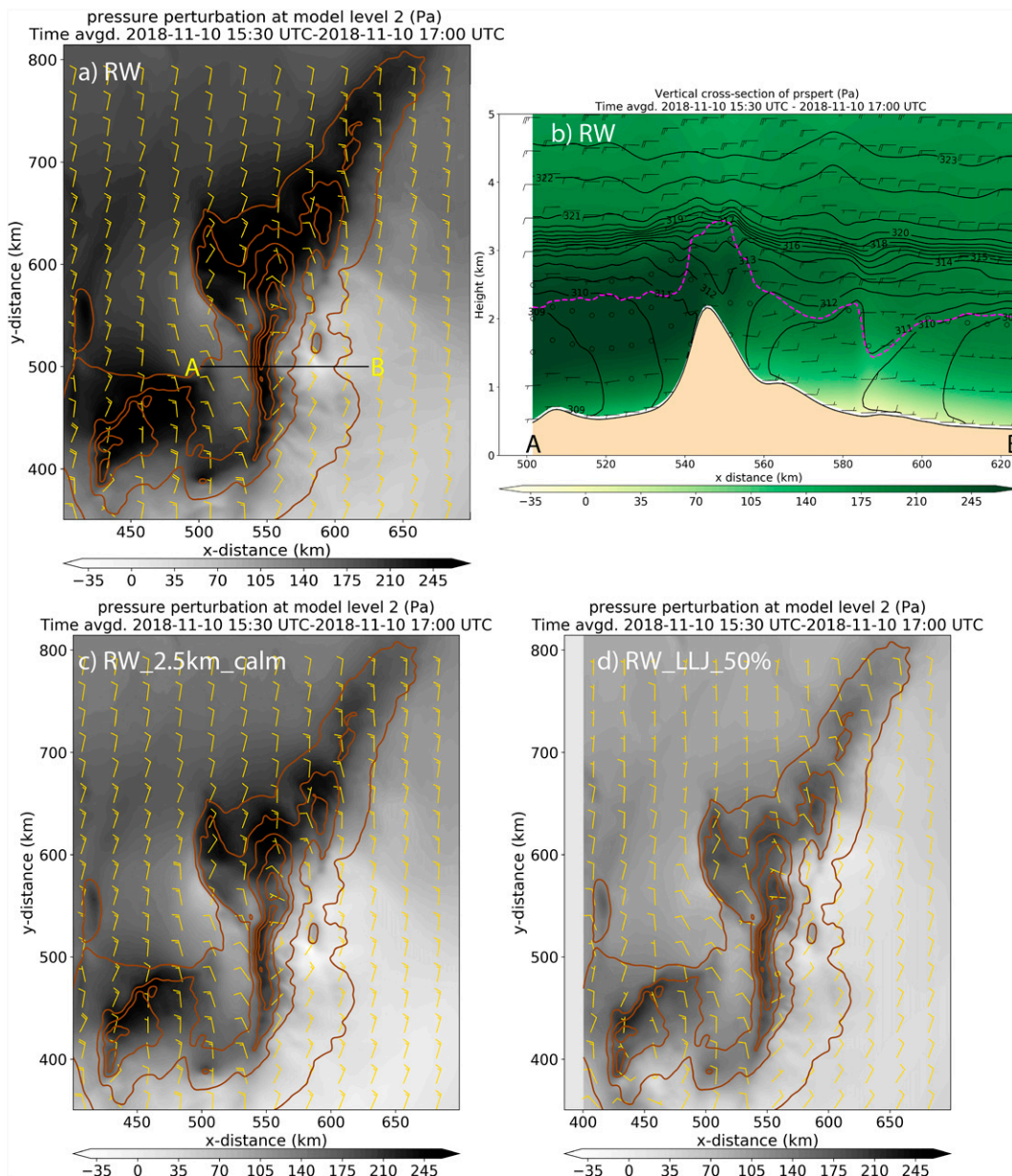


FIG. 6. Time-averaged (1530–1700 UTC) pressure perturbation (Pa; shaded) at model level 2 (~150 m AGL) and 10-m winds (barbs) for experiment (a) RW, (c) RW_2.5km_calm, and (d) RW_LLJ_50%. (b) Vertical cross section of time-averaged pressure perturbation (Pa; shaded) and potential temperature (solid black contours) along transect AB marked in (a) for RW. Also shown in (b) is the time-averaged height of the PBL. Terrain contours (m) in (a), (c), and (d) are shown in brown. The topography in (b) is shown in light brown color.

the main ridge, roughly confined between Sierra de Pocho and northern Sierras Chicas which lie to the west and east of the main ridge, respectively. The parcels continue southward and then toward the mountain top, and ultimately some of them arrive at the convergence zone (solid green contours in Fig. 7 represent low-level mass convergence values of 0.002 s^{-1}). The parcels in stream B (western branch) stay relatively close to the high terrain while many parcels in stream C (eastern branch) traverse a longer distance with a larger

radius of curvature before entering the convergence zone. This could be the result of stronger northerly flow over the eastern slopes, as shown by time-averaged 10-m winds in Fig. 5a. The higher strength of winds over the east side of the ridge relative to the west side could be attributed to a stronger north–south pressure gradient over the eastern slopes (Fig. 6a). It is clear from Fig. 7a that low-level parcels on the west side of the ridge experience eastward acceleration while those over the east side experience westward acceleration due to the pressure

u-wind momentum terms along backward trajectories starting at 150m AGL over the ridge at 1700 UTC for RW

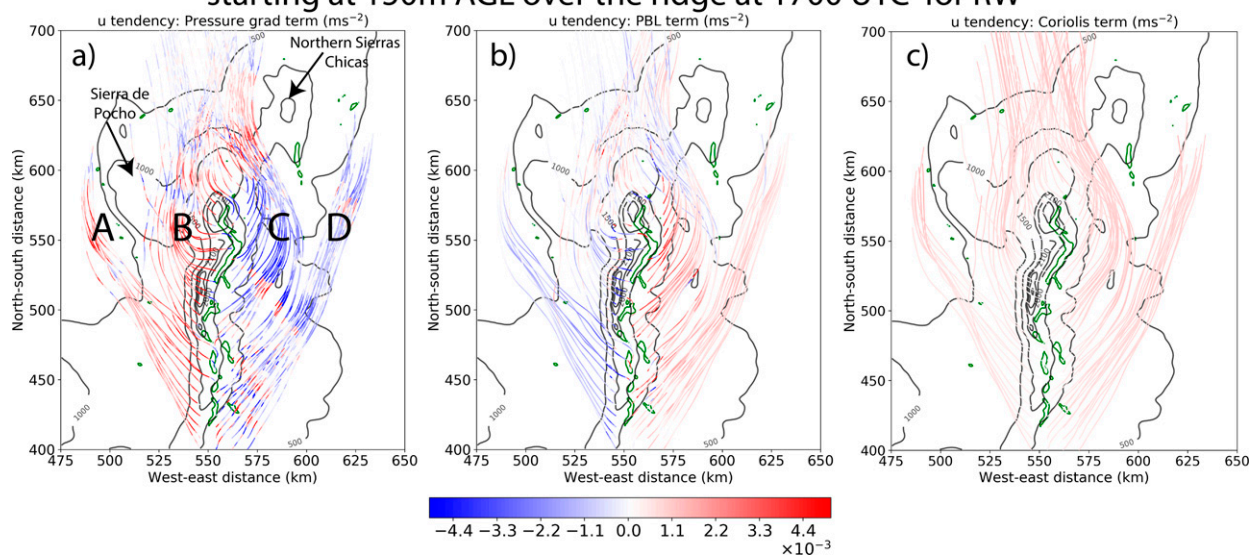


FIG. 7. Values of various terms (m s^{-2}) contributing to the u -wind tendency along backward trajectories of parcels starting at model level 2 at 1700 UTC: (a) pressure gradient term, (b) PBL term, and (c) Coriolis term. Solid black contours represent terrain height (m); solid green contours represent mass convergence (at model level 2) values of 0.002 s^{-1} . The incoming parcels are divided into four streams: A, B, C, and D in (a).

gradient forces resulting from a combination of the flow blocking (purely dynamic effect) and diabatic heating of the terrain. The western branch experiences strong westerly acceleration over the ridgetop before descending and decelerating over the eastern slopes. The PBL term, in general, opposes the motion, while the Coriolis term accelerates the northerly flow eastward. Other implicit and explicit diffusion terms that contribute to zonal acceleration are negligible.

The convergence line in RW appears around 2 h into the simulation (1330 UTC) and is sustained until 2200 UTC with little movement in the east–west direction. The persistence of the convergence line indicates that an area of sustained mesoscale ascent exists within the PBL. Figure 8 shows a vertical cross section of time-averaged vertical velocity, water vapor mixing ratio, along-plane winds, and PBL height for all the experiments along a transect marked as AB in Fig. 6a. All the experiments show upslope flow (e.g., Geerts et al. 2008; Kirshbaum and Wang 2014) and the resulting updrafts over both western and eastern slopes as well as upslope moisture advection. Experiment R shows the most symmetric distribution of potential temperature, moisture, and winds. The principal rising branch of the circulation in RW (which coincides with convergence line in Fig. 5a) lies over the eastern slopes. Vertical motion within this convergence line contributes to the erosion of CIN, and CI occurs around 1710 UTC in the control simulation.

The present study bears some similarity in its methodology and results to Wang et al. (2016), who investigated physical processes involved in a late morning CI event over an eastward extending ridge of the Dabie Mountains in the Anhui

region of China by using a series of numerical simulations with data assimilation. They found that thermally driven upslope flows, dynamically driven lee-side convergence, and flow in the north–south oriented valleys between various peaks values led to the formation of a larger primary convergence line. CI took place in smaller regions of enhanced convergence within this primary convergence line; these regions showed superposition of two or more of these convergence causing mechanisms. However, unlike in Wang et al. (2016), we will show that mass convergence alone does not decide the location of CI and that the mesoscale distribution of moisture around the ridge is also important.

Figure 8a also shows significant gravity wave activity above the synoptic inversion. Previous research (Bhushan and Barros 2007; Siller et al. 2019) has indicated the potential role of gravity wave induced leeside convergence and hydraulic jumps as a possible mechanism of initiation of deep moist convection. However, we find that it is unlikely that deep gravity waves played any major role in CI as the simulation RW_2.5km_calm has a convergence line over the eastern slopes, similar to that in RW (Figs. 5c, 8e). CI occurred in RW_2.5km_calm in the southeast quadrant around 1620 UTC, i.e., earlier as compared to RW (1710 UTC). This shows that the low-level/subridge thermodynamic and kinematic environment plays a bigger role in setting up the thermal circulation and producing the initial updrafts, and gravity waves above the mountain do not assert a significant influence. It is possible that gravity waves alter the specific timing of CI by reinforcing or suppressing the boundary layer upward motion at different times depending on their phase.

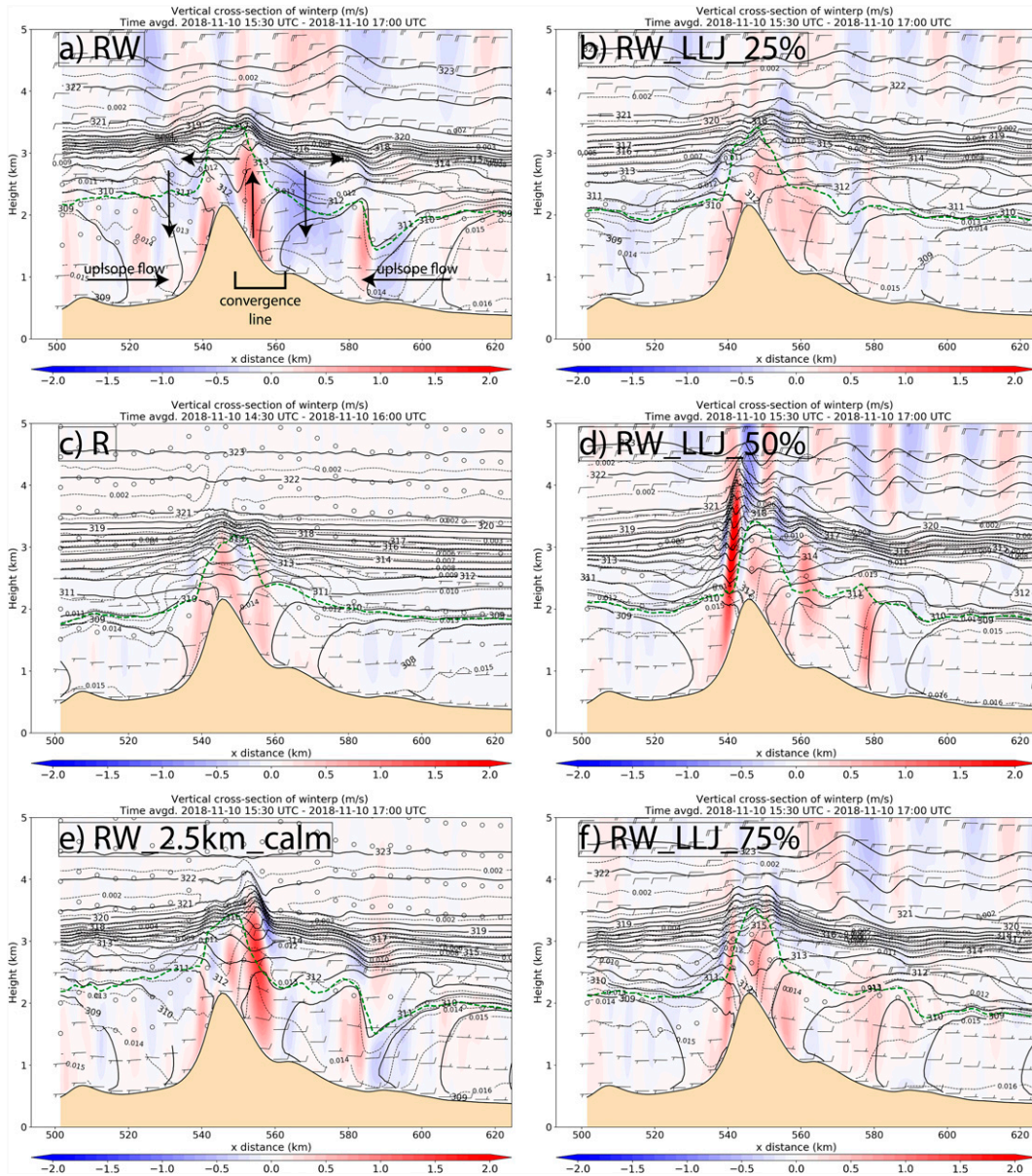


FIG. 8. Vertical cross sections of time-averaged vertical velocity (m s^{-1} ; shaded), potential temperature (K; solid black contours), water vapor mixing ratio (kg kg^{-1} ; black dashed contours), in-plane winds (knots; barbs), and PBL height (m; dashed green contours) for experiment (a) RW, (b) RW_LLJ_25%, (c) R, (d) RW_LLJ_50%, (e) RW_2.5km_calm, and (f) RW_LLJ_75% along transect AB (horizontal black line in Fig. 6a). The duration for time averaging is 1530–1700 UTC for all experiments except R, where it is 1430–1600 UTC. The topography is shown in light brown color. For the barbs a half barb = 5 kt, a full barb = 10 kt, and a pennant = 50 kt. Hollow circles imply very weak or no winds.

Figure 9a shows the cloud field over the simulated convergence line, with the southern half of the line showing increasingly growing clouds being sheared toward the southeast direction. The 1600 UTC outgoing longwave and visible (red band) radiance imagery from GOES-16 satellite also shows a developing line of cumuli over the SDC (Figs. 9b,c). Another similarity between the model results and the satellite imagery is the lack of cloud field over the region encircled in red

(Figs. 9a–c). In the analysis conducted in section 2, no CI events were observed over this region for environments with LLJ (Fig. 2b), and as shown later, this region exhibits high values of surface-based CIN (SBCIN) throughout the duration of the control simulation. It is important to note that all aspects of these quasi-idealized simulations of CI cannot be directly compared with the IOP4 observations. As mentioned earlier, the simulations in this study are used to explain the

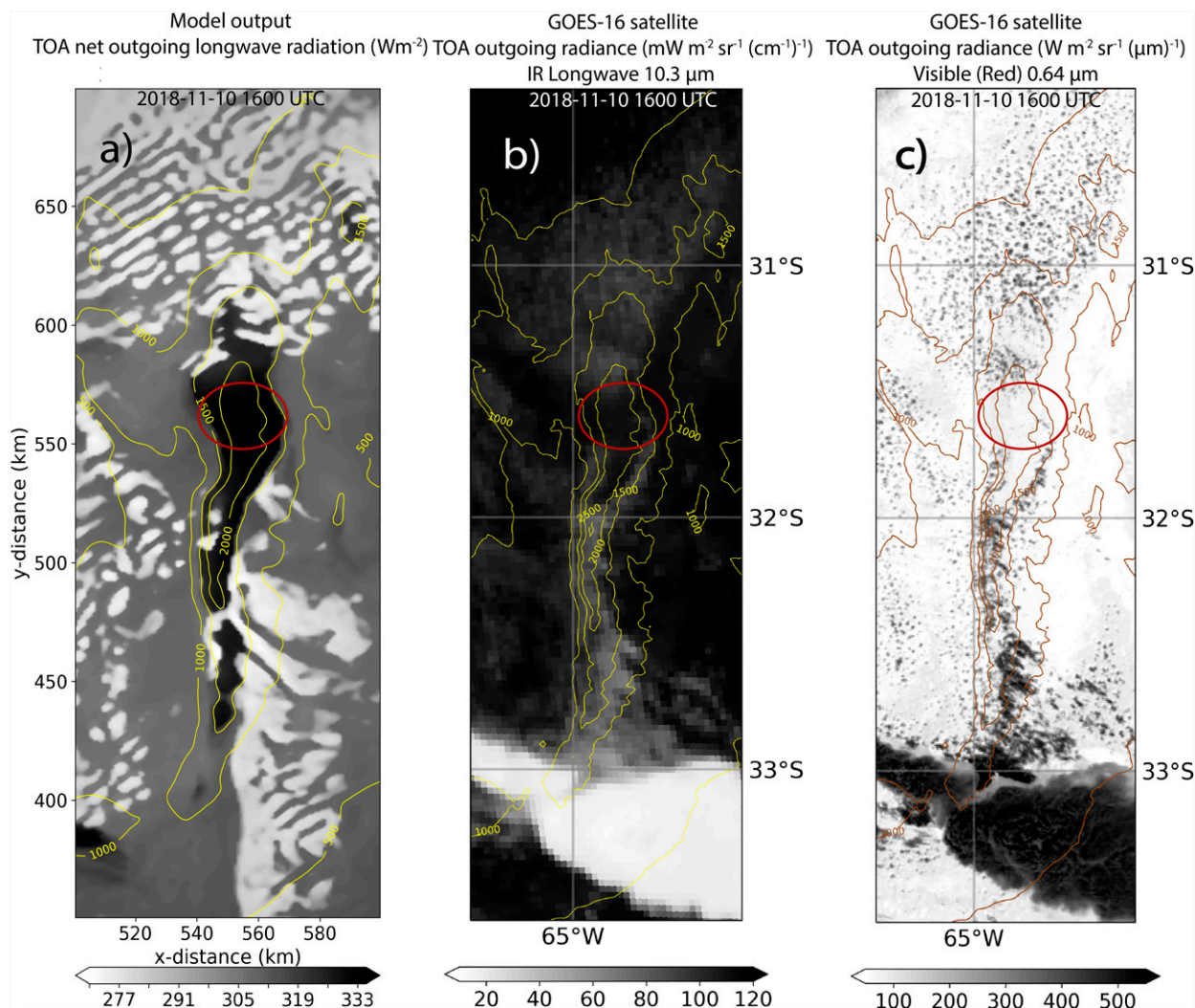


FIG. 9. (a) Top of the atmosphere (TOA) outgoing longwave radiation (W m^{-2} ; shaded) at 1600 UTC from model output, (b) TOA outgoing IR longwave radiance [$\text{mW m}^{-2} \text{sr}^{-1} (\text{cm}^{-1})^{-1}$; shaded] from channel 13 of *GOES-16* at 1600 UTC 10 Nov 2018, (c) TOA outgoing visible (red) radiance ($\text{W m}^{-2} \text{sr}^{-1} \mu\text{m}^{-1}$; shaded) from channel 2 of *GOES-16* for the same time as (b). The yellow contours in (a) and (b) and brown contours in (c) represent terrain height. Note that the yellow contours in (a) represent the terrain used in the model and are smoother in comparison to the contours in (b) and (c).

climatology of CI occurrence around the SDC and not to simulate IOP4 events. However, the similarity between the model output and IOP4 observations with respect to the cloud field over the convergence line, which is one of the major subjects of investigation in this study, instills confidence in the representativeness of the simulations. At the same time, the relative coarseness of the various features present in the model simulation is quite evident. For instance, the satellite imagery shows cellular convection toward the north of the ridge, while the model output shows horizontal roll-like convection over this location. As mentioned in section 3, this difference could arise from several factors, including the inability of the model to resolve PBL eddies with a horizontal grid spacing of 1 km (Bryan et al. 2003).

b. Terrain-induced vertical wind shear enhancement

An important consequence of the presence of near-surface, easterly upslope flow over the eastern slopes and westerly flow aloft in RW is strong vertical wind shear over these slopes (Fig. 10). A narrow (<50-km width) band of 0–6 km AGL westerly vertical wind shear with magnitude between 50 and 60 kt can be observed over the eastern slopes; the shear decreases toward east. These results are similar to those presented by Trapp et al. (2020), who use 1800 UTC radiosonde data from IOP4 to show that a corridor of strong vertical wind shear exists east of the ridgeline. They show that the magnitude of 0–6-km shear is around 58 kt close to the high terrain (similar to the magnitudes seen in the RW simulation) and decreases from west to east, further validating the results

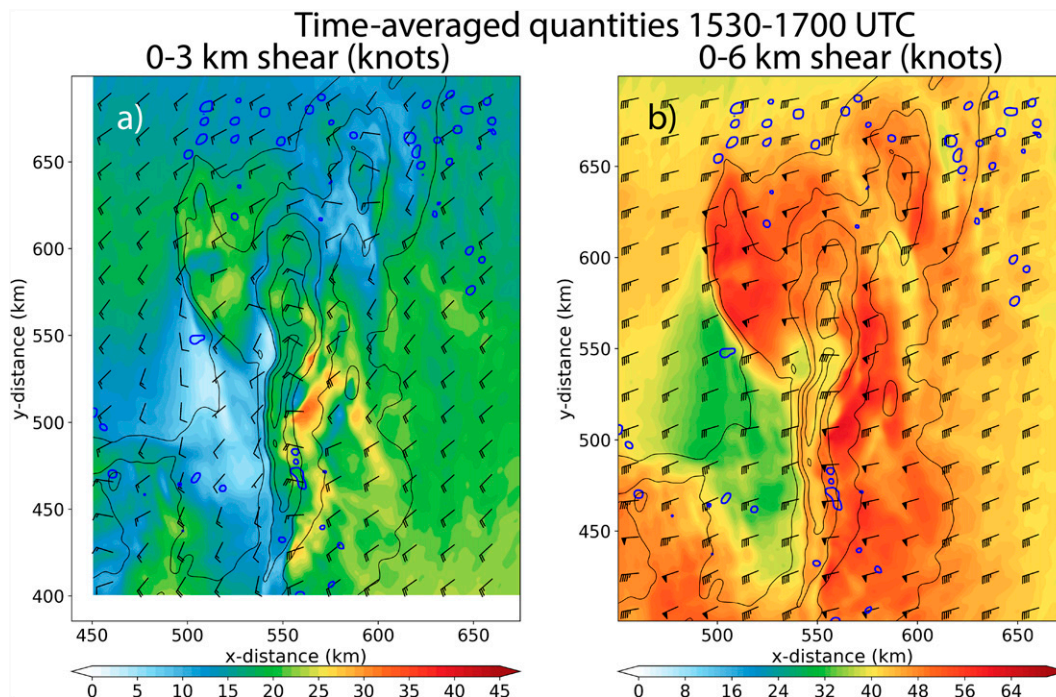


FIG. 10. The 1530–1700 UTC time-averaged (a) 0–3-km vertical wind shear (knots; shaded and barbs) and (b) 0–6-km vertical wind shear (knots; shaded and barbs). The dashed blue contours in (a) and (b) represent the 35-dBZ reflectivity values at model level 1 at 1700 UTC. Terrain height (m) is shown by solid black contours. For the barbs, a half barb = 5 kt, a full barb = 10 kt, and a pennant = 50 kt.

presented in this study. Their analysis of radar observations for IOP4 shows that the mesocyclone associated with the east-moving supercell produced during IOP4 lasted around 25 min. They hypothesize that the short residence time of the supercell within the narrow zone of enhanced shear could have contributed to the short life of the mesocyclone. Additionally, they propose that the locally enhanced shear could potentially create wider updrafts (Mulholland et al. 2020) which would lead to wider, colder downdrafts and, therefore, deeper cold pools (Marion and Trapp 2019), consequently leading to faster upscale growth and secondary CI.

The terrain-enhanced shear seen in RW has potential implications for CI occurrence over the convergence line, too. As described earlier, CI in RW_2.5km_calm (little deep layer shear) takes place about 40 min prior to CI in RW (deep layer shear of ~58 kt). Convective cells in RW develop into supercells (evolution of one such cell described in 4d) that move eastward, off the higher terrain, while cells in RW_2.5km_calm move southward along the convergence line.

While deep layer vertical wind shear is similar in all the LLJ modification experiments, low-level vertical wind shear decreases as LLJ strength decreases (now shown). Again, this could have consequences for updraft growth via mechanisms such as entrainment. A detailed analysis of the same will be presented in a future paper. Besides modulating vertical wind shear, the interaction of the background flow with the heated mountain strongly influences moisture distribution.

c. Mesoscale distribution of moisture around the SDC

Figure 11 shows water vapor mixing ratio at the lowest model level for various experiments. Domainwide moisture increases as the LLJ strength increases (increased surface moisture fluxes). One could also observe increasingly larger patches of drier air along the western and eastern slopes as LLJ strength increases. In the simulation with LLJ strength reduced to 25% of the RW level (essentially, no LLJ), CI occurs at two locations along the convergence line over the eastern slopes (see 35-dBZ reflectivity contours enclosed in red circles in Fig. 11d). For the rest of the experiments, all of which include an LLJ, the CI location lies in the southeast quadrant of the main ridge. It appears that the suppression of CI along the northern portion of the convergence line by the dry air helps in focusing CI in the SE quadrant in experiments that include an LLJ. This is also reflected in CIN values (Fig. 12), which are reduced to near zero over the southern part of the eastern slopes in RW, RW_2.5km_calm, RW_LLJ_50%, and RW_LLJ_75%, where both mass convergence (Fig. 5) and higher moisture values are present (Fig. 11). The southern portion of the eastern slopes in these experiments also exhibits high surface-based CAPE (SBCAPE) values (Fig. 13), near-surface equivalent potential temperature (θ_e) values (>357 K; not shown), and higher values of moisture flux convergence vertically integrated over the depth of the PBL (not shown; Banacos and Schultz 2005; Shepherd et al. 2001). Thus, CI occurs preferentially over this high CAPE and high θ_e region of the line, where both mechanical lift from the

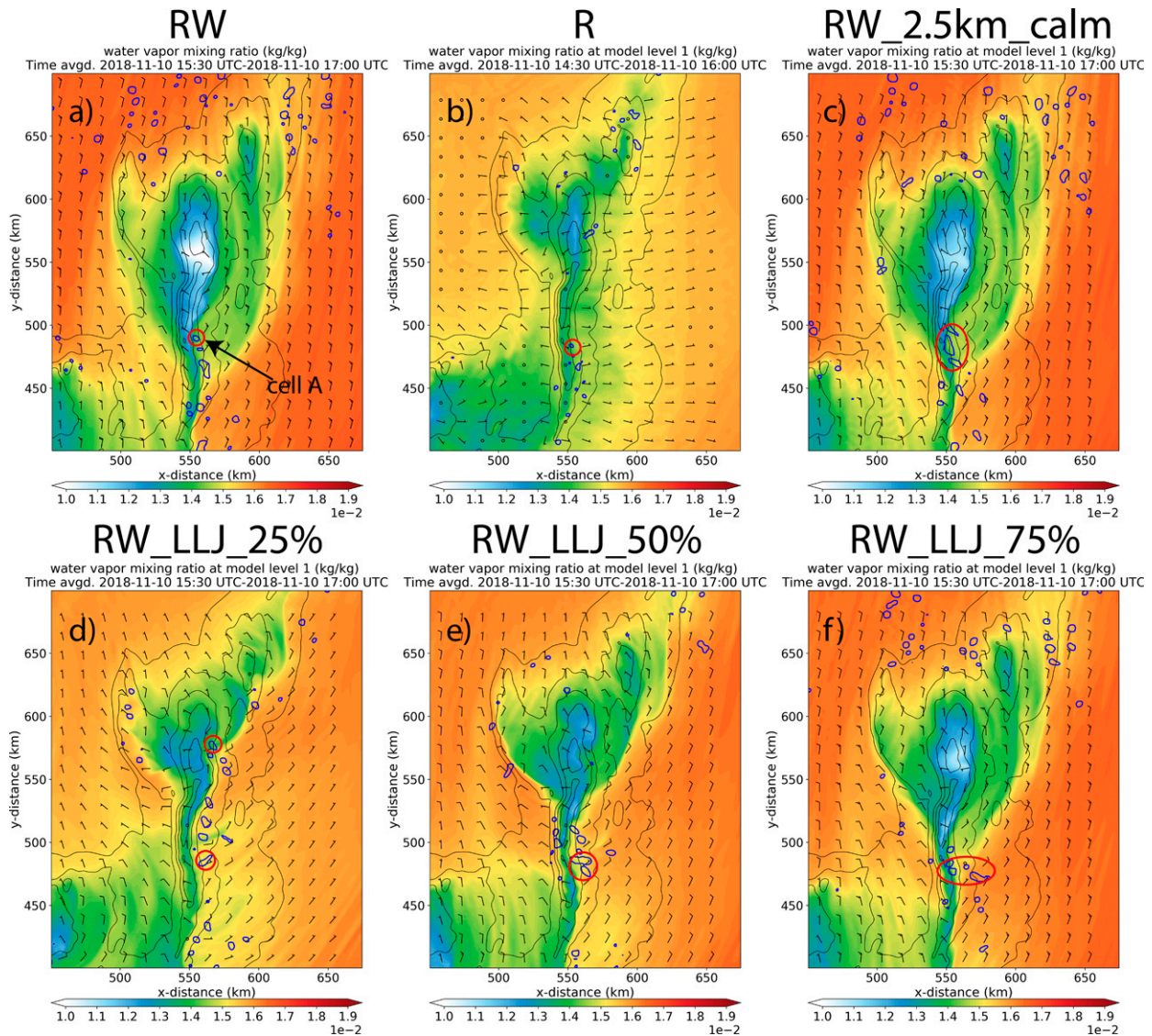


FIG. 11. The 1530–1700 UTC time-averaged mixing ratio (kg kg^{-1} ; shaded) and 10-m wind (barbs) for simulation (a) RW, (b) R, (c) RW_2.5km_calm, (d) RW_LLJ_25%, (e) RW_LLJ_50%, and (f) RW_LLJ_75%. The terrain height is shown in all the panels with solid black contours. Solid blue contours represent 35-dBZ model-simulated reflectivity at the lowest model level at 1710 UTC for RW, 1600 UTC for R, and 1700 UTC for the rest of the experiments. Red circles show the cells that develop into deep moist convection (CI events). For the barbs, a half barb = 5 kt, a full barb = 10 kt, and a pennant = 50 kt.

convergence and favorable thermodynamic forcing from moisture availability are present. These results are reminiscent of Kovacs and Kirshbaum (2016) in which the authors found strong, topographically induced mesoscale variability in the occurrence of deep moist convection over southern Quebec, Canada. They attributed the existence of various convection maxima in the region to strong mass and moisture convergence at the junction of river valleys and over the leeside of mountains, with these locations showing increased values of PBL moisture and CAPE and decreased values of CIN.

Trajectory analysis is used to further understand the distribution of moisture around the SDC. Figure 14 shows the values of water vapor mixing ratio of air parcels along their

trajectories as they arrive at the convergence zone for RW and RW_LLJ_50% experiments. Considering Fig. 14a first, we observe that parcels in streams B and C are less moist than parcels in streams A and D. Streams B and C coincide with the drier areas on both sides of the main ridge. The parcels in these streams arrive from the north of the ridge while parcels in the moister streams A and D arrive from the northwest and northeast directions, respectively. Similar pattern occurs in LLJ_RW_50% (Fig. 14b), but in this case, streams A and D lead to the formation of most of the convergence line. Figure 15 shows the water vapor mixing ratio values and height (MSL) for select parcels in each stream for RW (dashed boxes in Fig. 14a). Interestingly, parcels in streams B

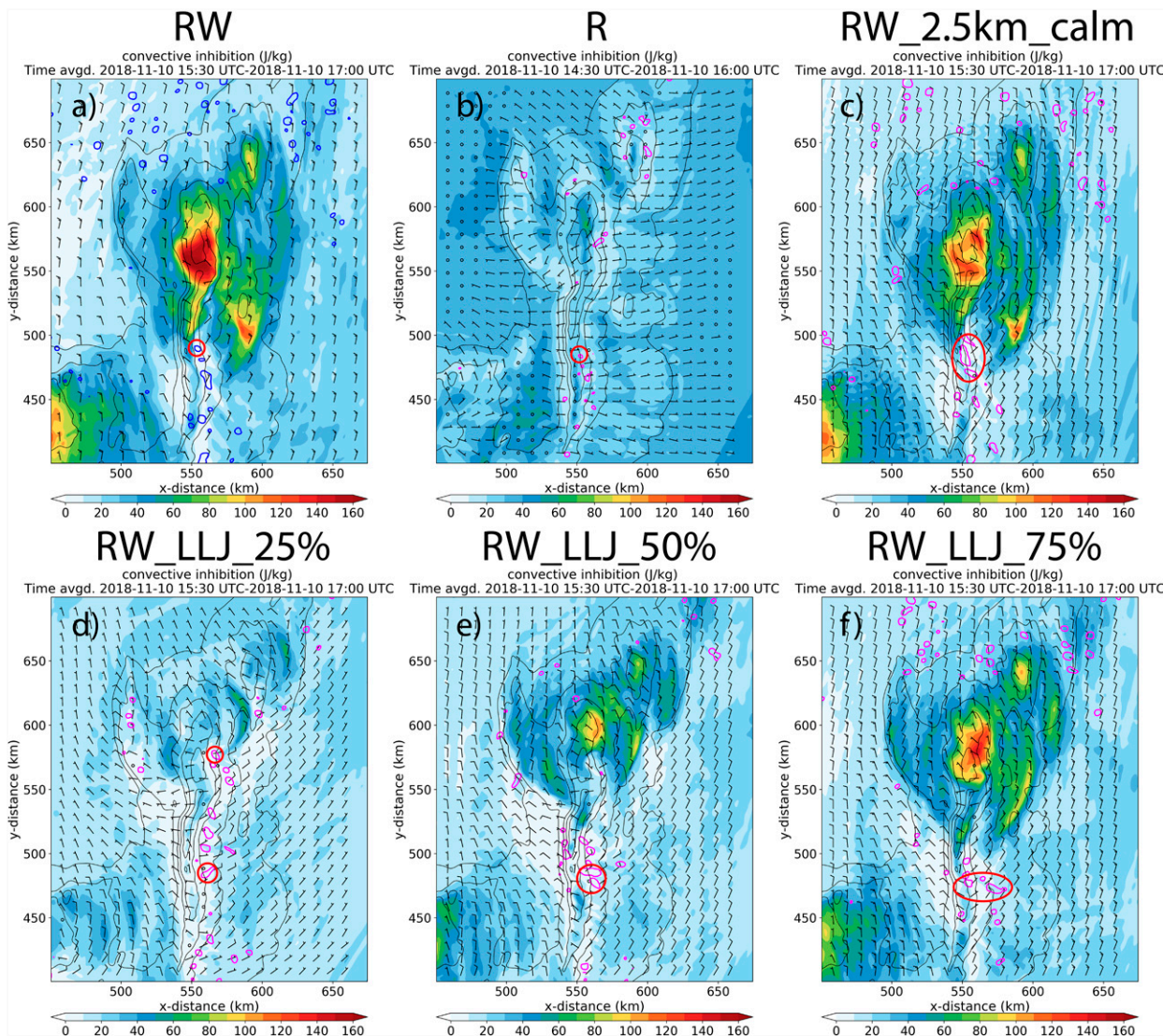


FIG. 12. As in Fig. 11, but for CIN ($J\ kg^{-1}$).

and C that arrive at the convergence line area at 1700 UTC around 150 m AGL originate over a much larger depth within the lower atmosphere, with a vast majority of these parcels coming from 1 to 2.5 km MSL; this explains their low moisture values. Many parcels in stream B descend as they cross the region between Sierra de Pocho and the main ridge; similarly, many parcels in stream C descend as they cross the gap between northern Sierras Chicas and the main ridge. Contrastingly, parcels in streams A and D do not show a wide variation in their height of origin and stay relatively close to the ground along their entire trajectories. This explains why they are moister than parcels in streams B and C. Similar results are obtained for all other experiments in the RW group (not shown).

An analysis of temperature field shows no major differences in low-level temperature and stability values among various experiments in the RW group (not shown). In

conclusion, we argue that it is the mesoscale distribution of moisture field that plays a dominant role in determining the location of CI within the larger convergence line spanning the length of the main ridge. CI occurs around the same location in RW, RW_LLJ_75%, and RW_LLJ_50%. It is hard to ascertain the precise dependence of CI location on LLJ strength based on the experiments conducted in this study.

Figure 11a shows numerous convective cells (35-dBZ reflectivity contours) to the north of the SDC ($y > 650$ km) in RW. We reiterate that for the purposes of this study, these cells do not constitute CI as none of them develop into deep moist convection; they are short-lived, shallow showers. Many cloud-resolving models produce overly strong updrafts and excessive amount of large ice, and this could lead to early production of precipitation and therefore incorrectly high reflectivity values (Stanford et al. 2019; Varble et al. 2020).

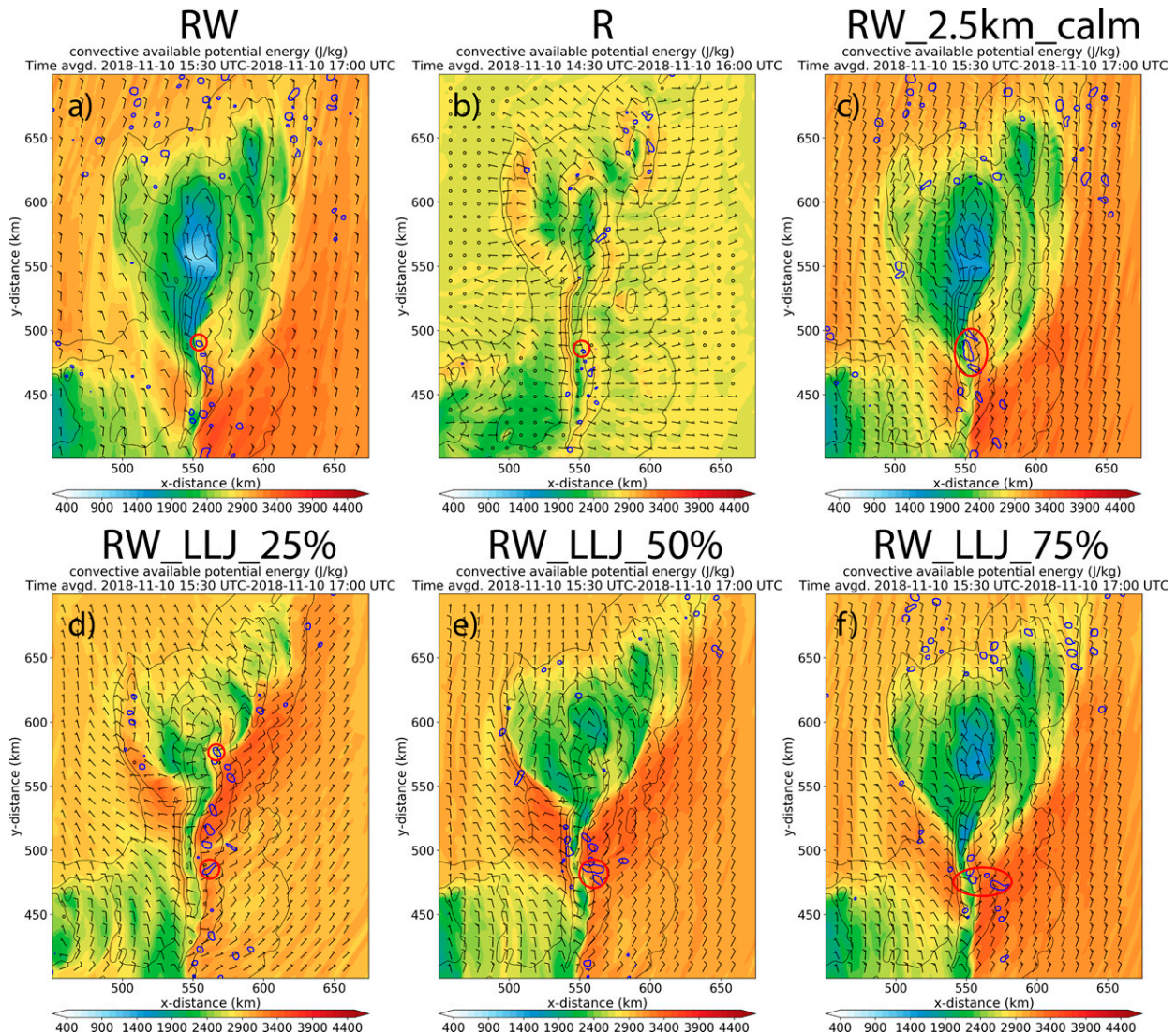


FIG. 13. As in Fig. 11, but for CAPE (J kg^{-1}).

Several short-lived cells also appear between 1500 and 1700 UTC over the southern portion of the convergence zone in RW. CI in this simulation occurs around 1710 UTC (first appearance of the 35-dBZ reflectivity echo) as a cell (hereafter cell A; Fig. 11a) forms and then moves southeastward over the eastern slopes, ultimately growing into an eastward-moving supercell-like storm. Subsequently, several other cells originating from very close to the genesis point of cell A appear one after the other. They follow similar paths and grow into eastward-moving supercell-like storms, in general, lasting longer than cell A. However, none of these cells travel further than 75 km from the point of initiation. They dissipate close to the 1000-m terrain height contour as CIN increases eastward of this terrain contour (Fig. 12a). This region of CI lies in the southeast quadrant of the main ridge and overlaps with the general area of frequent CI occurrence in observations, as described in section 2. Four other simulations

identical to RW in all respects but initialized with different random perturbations in the potential temperature field (RW_ENS1, RW_ENS2, RW_ENS3, RW_ENS4) show CI around the same location and within ten minutes of 1710 UTC (not shown). The evolution of the storms in these four simulations as they cross the eastern slopes is also similar to that in RW.

As far as the western slopes of the main ridge are concerned, areas that receive air parcels within stream A also show low SBCIN values (Fig. 12a). However, deep moist convection does not initiate over this region in RW. The lift in this region is not strong and deep enough to cause CI (Fig. 5a). However, CI does occur over western slopes in all the reduced LLJ strength experiments, with some cells even initiating over the western slopes (not shown), crossing the ridgeline, and moving eastward while traversing the eastern slopes.

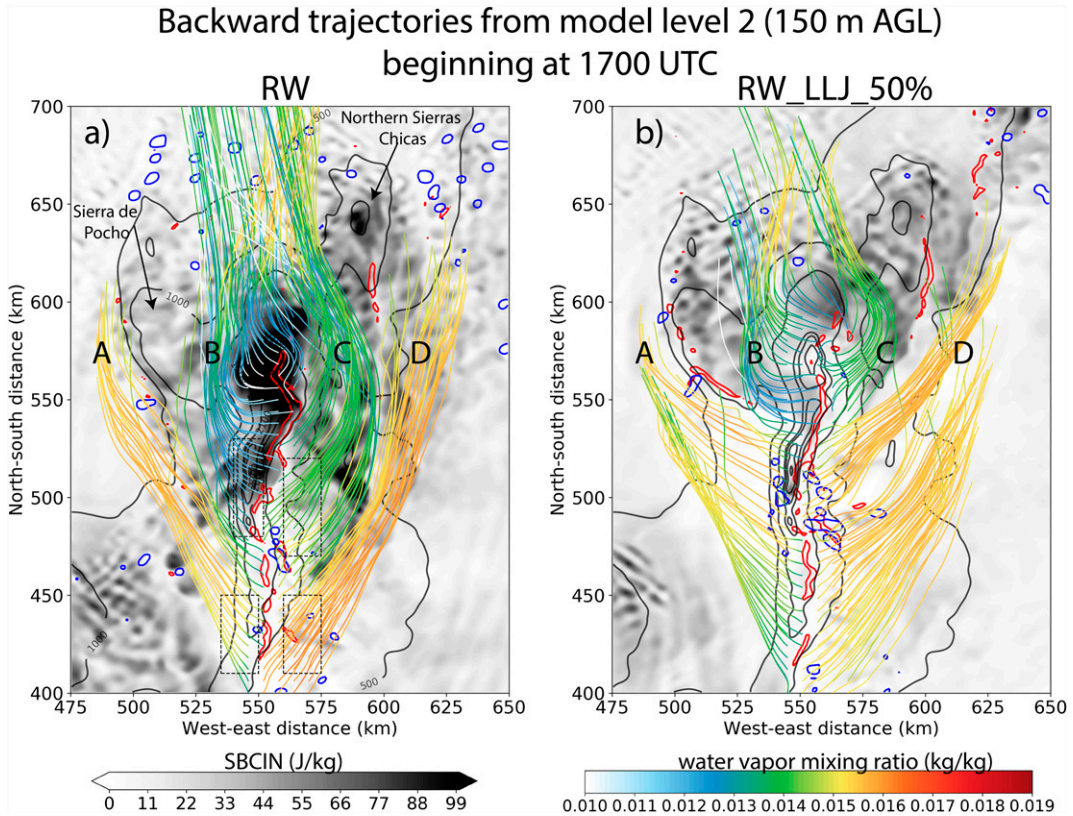


FIG. 14. Mixing ratio (kg kg^{-1}) values along backward trajectories of parcels starting at model level 2 at 1700 UTC for (a) RW and (b) RW_LLJ_50%. Solid black contours represent terrain height (m). Red contours represent 0.002 s^{-1} mass convergence contours at model level 2 at 1700 UTC. Solid blue contours represent 35-dBZ reflectivity values at model level 1 at 1700 UTC. Gray shaded contours represent SBCIN at 1700 UTC. The incoming parcels are divided into four streams: A, B, C, and D. The four boxes in (a) show the four regions, each one in a different stream, whose parcel properties are shown in Fig. 15.

d. Evolution of initial updrafts in the control simulation

Figure 16 shows the time evolution of the updraft of cell A (Fig. 11a) via vertical cross sections of vertical velocity, water vapor mixing ratio, and potential temperature along moving transects passing through the translating updraft. The updraft begins as a region of sustained upward motion (Fig. 16a), growing gradually, as moist air is advected upslope into the inflow of the updraft. Upward motion within the convergence

line has existed over this location since 1330 UTC. Several studies point to the role of PBL eddies in focusing the exact location of CI within regions of reduced CIN (Weckwerth et al. 2008; Trier et al. 2015). It takes about 50 min for the updraft to reach the height of 5 km MSL from the initial height of 3.5 km MSL (Figs. 16a–d).

As the updraft grows, it tilts eastward in the strongly sheared environment (Figs. 16d,e). This tilting may lead to

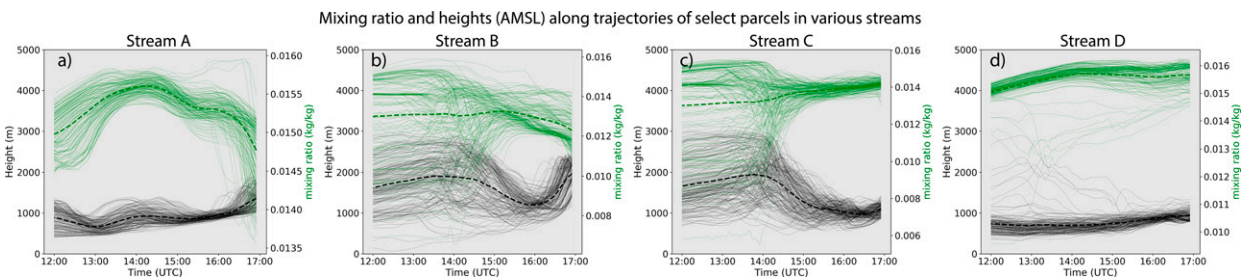


FIG. 15. Time series of water vapor mixing ratio (kg kg^{-1} ; green lines, dashed line is the mean) and height MSL (m; black lines; dashed line is the mean) for select parcels along their trajectories in (a) stream A, (b) stream B, (c) stream C, and (d) stream D.

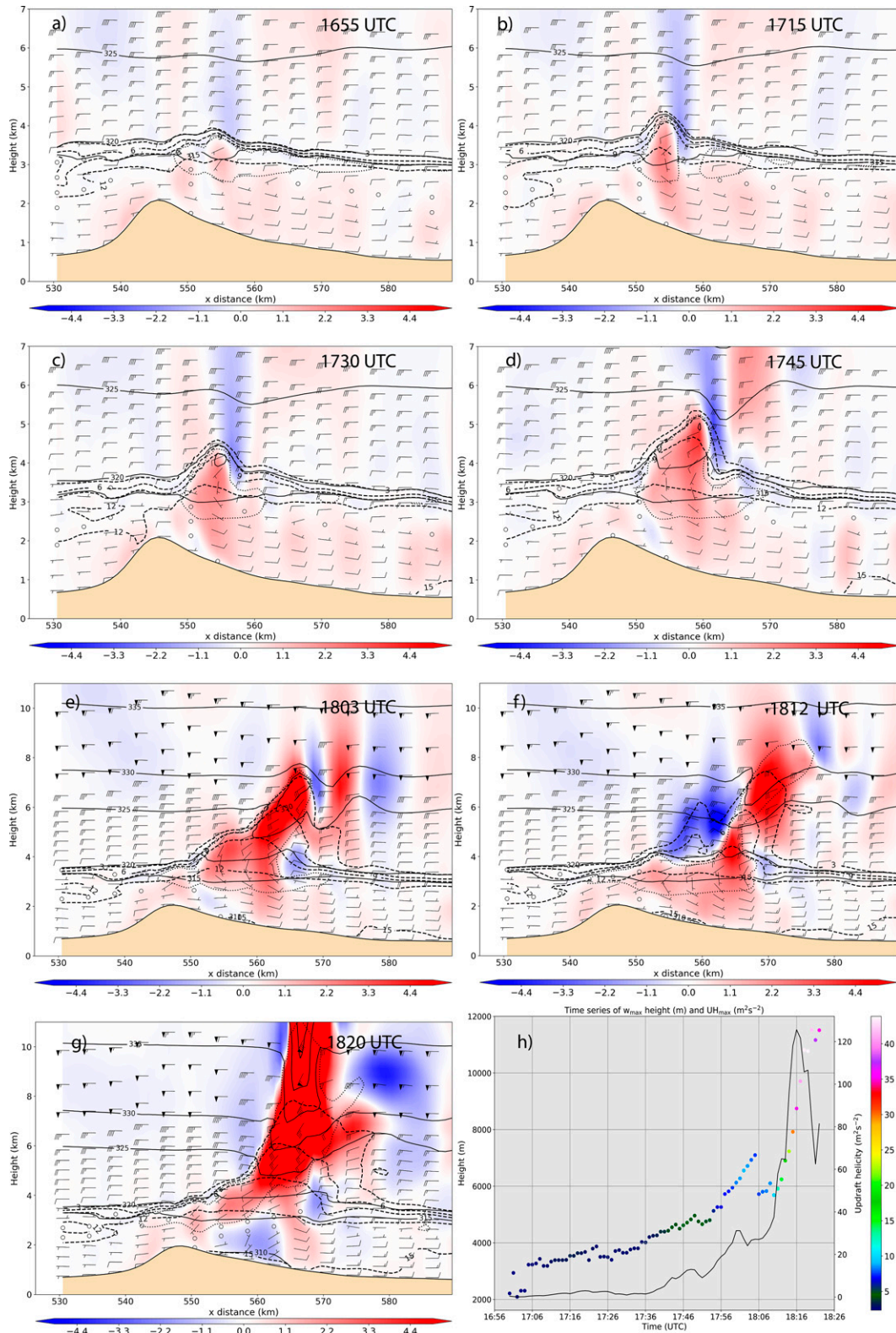


FIG. 16. (a)–(g) Vertical cross section of vertical velocity (m s^{-1} ; shaded), potential temperature (K; solid black contours), water vapor mixing ratio (g kg^{-1} ; black dashed contours), $0.0002 \text{ kg kg}^{-1}$ cloud water mixing ratio values (black dotted contours), and in-plane winds (knots; barbs) along moving transects passing through the updraft at different

increased entrainment of drier environmental air into the updraft (e.g., Weisman 1992; Markowski et al. 2006) in addition to enhanced downward-direction dynamic pressure acceleration (Peters et al. 2019), which, perhaps, slows its transition to deep convection. This is reflected in the time series of maximum vertical velocity within the updraft of cell A and the height at which this velocity is achieved (scatterplot in Fig. 16h). The magnitude of maximum updraft vertical velocity ranges from 1 to 5 m s⁻¹ for the first 50 min of updraft growth (from 1700 to 1750 UTC) and achieves a peak value of 37 m s⁻¹ around 1807 UTC at a height of 11.5 km MSL, indicating a slow transition from nascent upward motion to shallow convection and a relatively quick transition from shallow to deep convection. The updraft growth also involves seemingly complex interactions with an intensifying wave feature (1803 UTC; Fig. 16e). Around 1806 UTC, the maximum vertical velocity magnitude drops; soon after, regeneration of this updraft is observed as the vertical velocity begins increasing again.

The time series of maximum values of the magnitude of vertically integrated updraft helicity (2–5 km AGL; Kain et al. 2008) associated with this updraft follows a similar curve (black curve in Fig. 16h), achieving a maximum value of about 120 m² s⁻² around 1815 UTC. These values of updraft helicity point to the supercellular nature of cell A (Naylor et al. 2012). As discussed in section 4b, cell A lies in a narrow zone of strong terrain-enhanced vertical wind shear. This has potential implications for both the rotation within the updraft as well as the updraft size (Mulholland et al. 2020). As cell A moves southeastward, it crosses the eastern slopes into an area of increasing CIN. Updraft helicity magnitude also declines after 1816 UTC.

From 1800 to 1820 UTC (Figs. 16e–g), the updraft seems to draw air (and therefore moisture) from both the western and eastern slopes of the ridge. Given the different thermodynamic properties of the parcels over the two sides of the ridge (parcels on the western side are drier; Figs. 11a, 14a), this may have implications for updraft growth and sustenance, including cold pool formation. After 1820 UTC, the cell A updraft starts to interact with updrafts of other cells, and therefore, analysis past this time is not included.

As far as the simulation R is concerned, convective cells (model-simulated reflectivity at the lowest model level >35 dBZ) appear around 1530 UTC (not shown; earlier than RW) all over the ridgeline; some of these cells grow into deep moist convection and produce cold pools which cross the eastern slopes while others cross the western slopes, eventually causing secondary CI along the gust fronts. All the cells dissipate quickly as they rain into their updrafts. In RW_2.5km_calm, CI occurs around 1620 UTC (earlier than RW), with convection forming in the southeastern quadrant of the SDC and

moving southward. In RW_LLJ_25%, CI occurs around 1605 UTC over northern and southern portion of the convergence line. In RW_LLJ_50% and RW_LLJ_75%, CI occurs at 1620 and 1640 UTC, respectively, over the southeast quadrant of the ridge. In both these experiments, the initial updrafts evolve into supercells that, in contrast to RW, move northeastward, eventually becoming cold pool dominant. An exhaustive analysis of the evolution of convection for all the experiments will be presented in a future paper. Overall, we notice that CI occurs earlier in simulations with weaker LLJ and reduced vertical wind shear, but apart from R (no background flow) and RW_LLJ_25% (nonexistent LLJ), it occurs in the southeast quadrant of the SDC.

5. Summary and conclusions

This study aims to investigate the mesoscale flow around the Argentinian mountain range of Sierras de Córdoba, a hotspot of convection initiation, during a commonly observed convective environment that produces severe weather on the range's eastern slopes. This environment involves daytime heating of the mountain range, the SALLJ, and upper-level westerly flow. Analysis of the CI data compiled by Mulholland et al. (2018) revealed that about 44% of all cases of mountain-related, daytime CI had an LLJ. Additionally, these events are concentrated in the southeast quadrant of the main ridge of the SDC.

Cloud-resolving simulations using isolated topography of the SDC and a sounding derived from IOP4 of the RELAMPAGO field campaign were conducted to explore the mesoscale flow around the terrain, understand the physical mechanisms leading to CI in the region, and explain the observed spatial distribution of CI events around the terrain. This sounding was chosen as it features an LLJ and the synoptic situation during IOP4 resembled the canonical preconvective conditions for this region. The results from the control simulation (RW) show that the northerly low-level flow is largely blocked; the flow splits at the northern head of the main ridge of the SDC into western and eastern branches. Both branches curve toward the ridgeline as they experience pressure gradient force directed toward the mountain within the PBL. As the western branch crosses the ridgeline and arrives from over the ridgetop, it collides with the eastern branch over the eastern slopes, leading to the formation of a convergence zone there. A circulation is set up with the area of the lift over the convergence line and downward branches over the western and eastern slopes; the circulation is asymmetric about the ridgeline. Three other experiments similar to the control experiment with regard to model setup and initial thermodynamic profile but progressively decreasing LLJ strength are conducted (RW_LLJ_75%, RW_LLJ_50%, and RW_LLJ_25%). Another experiment with no flow above

←
times. (h) Time series of the height (m MSL; scatterplot) of the grid point containing the maximum value of vertical velocity (w_{\max} ; m s⁻¹) within the updraft and maximum updraft helicity magnitude (2–5 km; solid black line) associated with the updraft. The shading of the points in the scatterplot represents the value of w_{\max} at that point. For the barbs, a half barb = 5 kt, a full barb = 10 kt, and a pennant = 50 kt.

2.5 km MSL is also conducted (RW_2.5km_calm). Finally, an experiment with calm conditions is conducted (R). All these experiments include the diurnal cycle and surface heat and moisture fluxes. Barring R, all the experiments produce a convergence line on the eastern slopes. We speculate that the low-level northerly flow interacts with the asymmetric terrain of the SDC to produce a wake low on the east side of the main ridge. This sets up a pressure gradient across the two sides of the ridge and helps in shifting the convergence line over the eastern slopes. The fact that we see a convergence line over the eastern slopes in RW_2.5km_calm rules out the possibility of downward transfer of momentum contributing to the eastward shifting of the convergence line in this case.

Meanwhile, the southern portion of this convergence line is associated with higher values of moisture, CAPE, and vertically integrated moisture flux convergence and experiences a slow but significant reduction in SBCIN. Trajectory analysis of air parcels within the convergence line and close to the ground (~150 m AGL) around CI time (1710 UTC for the control simulation) revealed that in RW, the two northerly colliding streams of air (streams B and C in Fig. 14) that lead to the formation a major portion the convergence line consist of air parcels originating from north of the main ridge and a layer of depth of around 2.5 km. These parcels (many of them are from above the PBL) descend as they move southward and then into the convergence line, leading to the formation of dry “patches” on either side of the main ridge. Two other moister streams of air (A and D) originating relatively closer to the ground and arriving from the northwest and northeast directions also contribute to the convergence line formation over the southern portion of the ridge. As the LLJ strength decreases, the extent of the drier regions decreases as streams B and C do not advance southward as much. At the same time, the moister streams A and D now contribute to a larger portion of the convergence line. However, we do not notice a significant shift in the CI location when the LLJ is weakened but not removed.

CI occurs around 1710 UTC (1410 LT) over the southern portion of the convergence line in the control simulation. Four more simulations using the same model setup and sounding but using different perturbations in the initial potential temperature field produced CI around similar location within 10 min of 1710 UTC. The updraft in the control simulation moves slowly southeastward while remaining in a narrow zone of terrain-enhanced vertical wind shear, before finally developing into a storm with supercellular characteristics (2–5-km updraft helicity maximum magnitude of $120 \text{ m}^2 \text{ s}^{-2}$). Similar to control simulation, CI occurred in RW_2.5km_calm in the southeastern quadrant of the main ridge, albeit a little earlier than in RW (1620 UTC). This showed that deep gravity waves did not play a significant role in CI. CI in reduced LLJ strength experiments occurred earlier as well when compared to RW. Other than the RW_LLJ_25% experiment, CI did not occur over the northern portion of the convergence line and remained confined to the southeast quadrant of the SDC. We conclude that the low-level background flow

containing an LLJ, in conjunction with the upslope flows, leads to the formation of a convergence line on the eastern slopes and helps in focusing CI over the southeast quadrant of the main ridge of the SDC.

Future work will involve an analysis of the evolution of storms originating over the SDC in various experiments conducted in this study. Further work is also being done to understand the effects of model resolution on CI timing and location over the complex terrain of the SDC.

Acknowledgments. This work was possible due to the funding provided by the National Science Foundation (Grant AGS-1661799). A part of the work was done while the first author was visiting NCAR, Boulder, for the Advanced Student Program (ASP) Graduate Visitor fellowship. The authors thank Dr. George Bryan of NCAR for providing the CM1 code and Tom Gowan for his trajectory calculation code (available at: <https://github.com/tomgowan/trajectories>). The authors acknowledge the MetPy Python package (May et al. 2020), used for analyzing the model data. We are also thankful to NCAR and the National Center for Supercomputing Applications for providing computational resources. We also thank the three anonymous reviewers whose comments led to significant improvement in the manuscript. We thank all RELAMPAGO-CACTI participants.

Data availability statement. The numerical model output generated as part of this study is available upon request. All the information required to replicate the simulations, including the soundings used for initialization of CM1 and the namelist settings are available at <https://github.com/itinderjot>. All RELAMPAGO-related data are available at https://data.eol.ucar.edu/master_lists/generated/relampago/.

REFERENCES

- Anabor, V., D. J. Stensrud, and O. L. L. De Moraes, 2008: Serial upstream-propagating mesoscale convective system events over southeastern South America. *Mon. Wea. Rev.*, **136**, 3087–3105, <https://doi.org/10.1175/2007MWR2334.1>.
- Banacos, P. C., and D. M. Schultz, 2005: The use of moisture flux convergence in forecasting convective initiation: Historical and operational perspectives. *Wea. Forecasting*, **20**, 351–366, <https://doi.org/10.1175/WAF858.1>.
- Banta, R. M., 1984: Daytime boundary-layer evolution over mountainous terrain. Part I: Observations of the dry circulations. *Mon. Wea. Rev.*, **112**, 340–356, [https://doi.org/10.1175/1520-0493\(1984\)112<0340:DBLEOM>2.0.CO;2](https://doi.org/10.1175/1520-0493(1984)112<0340:DBLEOM>2.0.CO;2).
- , 1986: Daytime boundary layer evolution over mountainous terrain. Part II: Numerical studies of upslope flow duration. *Mon. Wea. Rev.*, **114**, 1112–1130, [https://doi.org/10.1175/1520-0493\(1986\)114<1112:DBLEOM>2.0.CO;2](https://doi.org/10.1175/1520-0493(1986)114<1112:DBLEOM>2.0.CO;2).
- , and Coauthors, 1990: *Atmospheric Processes over Complex Terrain*. W. Blumen, Ed., Amer. Meteor. Soc., 323 pp., <http://link.springer.com/10.1007/978-1-935704-25-6>.
- Bell, B., and Coauthors, 2020: ERA5 monthly averaged data on pressure levels from 1950 to 1978 (preliminary version).

- C3S CDS, accessed 18 November 2020, <https://cds.climate.copernicus.eu/cdsapp#!/dataset/reanalysis-era5-pressure-levels-preliminary-back-extension?tab=form>.
- Bhushan, S., and A. P. Barros, 2007: A numerical study to investigate the relationship between moisture convergence patterns and orography in central Mexico. *J. Hydrometeorol.*, **8**, 1264–1284, <https://doi.org/10.1175/2007JHM791.1>.
- Bryan, G. H., and J. M. Fritsch, 2002: A benchmark simulation for moist nonhydrostatic numerical models. *Mon. Wea. Rev.*, **130**, 2917–2928, [https://doi.org/10.1175/1520-0493\(2002\)130<2917:ABSFMN>2.0.CO;2](https://doi.org/10.1175/1520-0493(2002)130<2917:ABSFMN>2.0.CO;2).
- , J. C. Wyngaard, and J. M. Fritsch, 2003: Resolution requirements for the simulation of deep moist convection. *Mon. Wea. Rev.*, **131**, 2394–2416, [https://doi.org/10.1175/1520-0493\(2003\)131<2394:RRFTSO>2.0.CO;2](https://doi.org/10.1175/1520-0493(2003)131<2394:RRFTSO>2.0.CO;2).
- Cancelada, M., P. Salio, D. Vila, S. W. Nesbitt, and L. Vidal, 2020: Backward adaptive brightness temperature threshold technique (BAB3T): A methodology to determine extreme convective initiation regions using satellite infrared imagery. *Remote Sens.*, **12**, 337, <https://doi.org/10.3390/rs12020337>.
- Corsmeier, U., and Coauthors, 2011: Processes driving deep convection over complex terrain: A multi-scale analysis of observations from COPS IOP 9c. *Quart. J. Roy. Meteor. Soc.*, **137**, 137–155, <https://doi.org/10.1002/qj.754>.
- Durran, D. R., and J. B. Klemp, 1983: A compressible model for the simulation of moist mountain waves. *Mon. Wea. Rev.*, **111**, 2341–2361, [https://doi.org/10.1175/1520-0493\(1983\)111<2341:ACMFTS>2.0.CO;2](https://doi.org/10.1175/1520-0493(1983)111<2341:ACMFTS>2.0.CO;2).
- Fabry, F., 2006: The spatial variability of moisture in the boundary layer and its effect on convection initiation: Project-long characterization. *Mon. Wea. Rev.*, **134**, 79–91, <https://doi.org/10.1175/MWR3055.1>.
- Farr, T. G., and Coauthors, 2007: The Shuttle Radar Topography Mission. *Rev. Geophys.*, **45**, RG2004, <https://doi.org/10.1029/2005RG000183>.
- Geerts, B., Q. Miao, and J. C. Demko, 2008: Pressure perturbations and upslope flow over a heated, isolated mountain. *Mon. Wea. Rev.*, **136**, 4272–4288, <https://doi.org/10.1175/2008MWR2546.1>.
- Hagen, M., J. Van Baelen, and E. Richard, 2011: Influence of the wind profile on the initiation of convection in mountainous terrain. *Quart. J. Roy. Meteor. Soc.*, **137**, 224–235, <https://doi.org/10.1002/qj.784>.
- Hanley, K. E., D. J. Kirshbaum, S. E. Belcher, N. M. Roberts, and G. Leoncini, 2011: Ensemble predictability of an isolated mountain thunderstorm in a high-resolution model. *Quart. J. Roy. Meteor. Soc.*, **137**, 2124–2137, <https://doi.org/10.1002/qj.877>.
- Hersbach, H., and Coauthors, 2019: Global reanalysis: Goodbye ERA-Interim, hello ERA5. *ECMWF Newsletter*, No. 159, ECMWF, Reading, United Kingdom, 17–24, <https://www.ecmwf.int/node/19027>.
- Hong, S.-Y., Y. Noh, and J. Dudhia, 2006: A new vertical diffusion package with an explicit treatment of entrainment processes. *Mon. Wea. Rev.*, **134**, 2318–2341, <https://doi.org/10.1175/MWR3199.1>.
- Houze, R. A., Jr., 1993: *Cloud Dynamics*. Academic Press, 606 pp.
- Jiménez, P. A., J. Dudhia, J. F. González-Rouco, J. Navarro, J. P. Montávez, and E. García-Bustamante, 2012: A revised scheme for the WRF surface layer formulation. *Mon. Wea. Rev.*, **140**, 898–918, <https://doi.org/10.1175/MWR-D-11-00056.1>.
- JPL, 2014: NASA Shuttle Radar Topography Mission combined image data set. NASA EOSDIS Land Processes DAAC, accessed 20 November 2021, <https://doi.org/10.5067/MEaSURES/SRTM/SRTMMGM.003>.
- Kain, J. S., and Coauthors, 2008: Some practical considerations regarding horizontal resolution in the first generation of operational convection-allowing NWP. *Wea. Forecasting*, **23**, 931–952, <https://doi.org/10.1175/WAF2007106.1>.
- Kang, S.-L., G. H. Bryan, S.-L. Kang, and G. H. Bryan, 2011: A large-eddy simulation study of moist convection initiation over heterogeneous surface fluxes. *Mon. Wea. Rev.*, **139**, 2901–2917, <https://doi.org/10.1175/MWR-D-10-05037.1>.
- Kirshbaum, D. J., and C.-C. Wang, 2014: Boundary layer updrafts driven by airflow over heated terrain. *J. Atmos. Sci.*, **71**, 1425–1442, <https://doi.org/10.1175/JAS-D-13-0287.1>.
- Kottmeier, C., and Coauthors, 2008: Mechanisms initiating deep convection over complex terrain during COPS. *Meteor. Z.*, **17**, 931–948, <https://doi.org/10.1127/0941-2948/2008/0348>.
- Kovacs, M., and D. J. Kirshbaum, 2016: Topographic impacts on the spatial distribution of deep convection over southern Quebec. *J. Appl. Meteor. Climatol.*, **55**, 743–762, <https://doi.org/10.1175/JAMC-D-15-0239.1>.
- Labbouze, L., and Coauthors, 2013: Precipitation on the lee side of the Vosges Mountains: Multi-instrumental study of one case from the COPS campaign. *Meteor. Z.*, **22**, 413–432, <https://doi.org/10.1127/0941-2948/2013/0413>.
- Marion, G. R., and R. J. Trapp, 2019: The dynamical coupling of convective updrafts, downdrafts, and cold pools in simulated supercell thunderstorms. *J. Geophys. Res. Atmos.*, **124**, 664–683, <https://doi.org/10.1029/2018JD029055>.
- Markowski, P. M., and N. Dotzek, 2011: A numerical study of the effects of orography on supercells. *Atmos. Res.*, **100**, 457–478, <https://doi.org/10.1016/j.atmosres.2010.12.027>.
- , C. Hannon, and E. Rasmussen, 2006: Observations of convection initiation “failure” from the 12 June 2002 IHOP deployment. *Mon. Wea. Rev.*, **134**, 375–405, <https://doi.org/10.1175/MWR3059.1>.
- May, R. M., S. C. Arms, P. Marsh, E. Bruning, J. R. Leeman, K. Goebbert, J. E. Thielen, and Z. S. Bruick, 2020: MetPy: A Python package for meteorological data. GitHub, <https://github.com/Unidata/MetPy>.
- Morrison, H., G. Thompson, and V. Tatarskii, 2009: Impact of cloud microphysics on the development of trailing stratiform precipitation in a simulated squall line: Comparison of one- and two-moment schemes. *Mon. Wea. Rev.*, **137**, 991–1007, <https://doi.org/10.1175/2008MWR2556.1>.
- Mulholland, J. P., S. W. Nesbitt, R. J. Trapp, K. L. Rasmussen, and P. V. Salio, 2018: Convective storm life cycle and environments near the Sierras de Córdoba, Argentina. *Mon. Wea. Rev.*, **146**, 2541–2557, <https://doi.org/10.1175/MWR-D-18-0081.1>.
- , —, —, and J. M. Peters, 2020: The influence of terrain on the convective environment and associated convective morphology from an idealized modeling perspective. *J. Atmos. Sci.*, **77**, 3929–3949, <https://doi.org/10.1175/JAS-D-19-0190.1>.
- Naylor, J., M. S. Gilmore, R. L. Thompson, R. Edwards, and R. B. Wilhelmson, 2012: Comparison of objective supercell identification techniques using an idealized cloud model. *Mon. Wea. Rev.*, **140**, 2090–2102, <https://doi.org/10.1175/MWR-D-11-00209.1>.
- Nesbitt, S. W., and Coauthors, 2021: A storm safari in subtropical South America: Proyecto RELAMPAGO. *Bull. Amer. Meteor. Soc.*, **102**, E1621–E1644, <https://doi.org/10.1175/BAMS-D-20-0029.1>.

- Panosetti, D., S. Böing, L. Schlemmer, and J. Schmidli, 2016: Idealized large-eddy and convection-resolving simulations of moist convection over mountainous terrain. *J. Atmos. Sci.*, **73**, 4021–4041, <https://doi.org/10.1175/JAS-D-15-0341.1>.
- Peters, J. M., W. Hannah, and H. Morrison, 2019: The influence of vertical wind shear on moist thermals. *J. Atmos. Sci.*, **76**, 1645–1659, <https://doi.org/10.1175/JAS-D-18-0296.1>.
- Piersante, J. O., K. L. Rasmussen, R. S. Schumacher, A. K. Rowe, and L. A. McMurdie, 2021: A synoptic evolution comparison of the smallest and largest MCSs in subtropical South America between spring and summer. *Mon. Wea. Rev.*, **149**, 1943–1966, <https://doi.org/10.1175/MWR-D-20-0208.1>.
- Rasmussen, K. L., and R. A. Houze Jr., 2011: Orographic convection in subtropical South America as seen by the TRMM satellite. *Mon. Wea. Rev.*, **139**, 2399–2420, <https://doi.org/10.1175/MWR-D-10-05006.1>.
- , and —, 2016: Convective initiation near the Andes in subtropical South America. *Mon. Wea. Rev.*, **144**, 2351–2374, <https://doi.org/10.1175/MWR-D-15-0058.1>.
- , M. D. Zuluaga, and R. A. Houze Jr., 2014: Severe convection and lightning in subtropical South America. *Geophys. Res. Lett.*, **41**, 7359–7366, <https://doi.org/10.1002/2014GL061767>.
- Reinecke, P. A., and D. R. Durran, 2008: Estimating topographic blocking using a Froude number when the static stability is nonuniform. *J. Atmos. Sci.*, **65**, 1035–1048, <https://doi.org/10.1175/2007JAS2100.1>.
- Ribeiro, B. Z., and L. F. Bosart, 2018: Elevated mixed layers and associated severe thunderstorm environments in South and North America. *Mon. Wea. Rev.*, **146**, 3–28, <https://doi.org/10.1175/MWR-D-17-0121.1>.
- Romatschke, U., and R. A. Houze Jr., 2010: Extreme summer convection in South America. *J. Climate*, **23**, 3761–3791, <https://doi.org/10.1175/2010JCLI3465.1>.
- Rotach, M. W., and D. Zardi, 2007: On the boundary-layer structure over highly complex terrain: Key findings from MAP. *Quart. J. Roy. Meteor. Soc.*, **133**, 937–948, <https://doi.org/10.1002/qj.71>.
- Scheffknecht, P., S. Serafin, and V. Grubišić, 2017: A long-lived supercell over mountainous terrain. *Quart. J. Roy. Meteor. Soc.*, **143**, 2973–2986, <https://doi.org/10.1002/qj.3127>.
- Schneider, J. M., and D. K. Lilly, 1999: An observational and numerical study of a sheared, convective boundary layer. Part I: Phoenix II observations, statistical description, and visualization. *J. Atmos. Sci.*, **56**, 3059–3078, [https://doi.org/10.1175/1520-0469\(1999\)056<3059:AOANSO>2.0.CO;2](https://doi.org/10.1175/1520-0469(1999)056<3059:AOANSO>2.0.CO;2).
- Schwitalla, T., H. S. Bauer, V. Wulfmeyer, and G. Zängl, 2008: Systematic errors of QPF in low-mountain regions as revealed by MM5 simulations. *Meteor. Z.*, **17**, 903–919, <https://doi.org/10.1127/0941-2948/2008/0338>.
- Scott, D. W., 2015: *Multivariate Density Estimation: Theory, Practice, and Visualization*. 2nd ed. John Wiley and Sons, 384 pp.
- Shepherd, J. M., B. S. Ferrier, and P. S. Ray, 2001: Rainfall morphology in Florida convergence zones: A numerical study. *Mon. Wea. Rev.*, **129**, 177–197, [https://doi.org/10.1175/1520-0493\(2001\)129<0177:RMIFCZ>2.0.CO;2](https://doi.org/10.1175/1520-0493(2001)129<0177:RMIFCZ>2.0.CO;2).
- Siller, M., S. Serafin, and M. W. Rotach, 2019: Convection initiation in connection with a mountain wave episode. *EGU General Assembly*, Vienna, Austria, EGU, 9055.
- Soderholm, B., B. Ronalds, and D. J. Kirshbaum, 2014: The evolution of convective storms initiated by an isolated mountain ridge. *Mon. Wea. Rev.*, **142**, 1430–1451, <https://doi.org/10.1175/MWR-D-13-00280.1>.
- Stanford, M. W., H. Morrison, A. Varble, J. Berner, W. Wu, G. McFarquhar, and J. Milbrandt, 2019: Sensitivity of simulated deep convection to a stochastic ice microphysics framework. *J. Adv. Model. Earth Syst.*, **11**, 3362–3389, <https://doi.org/10.1029/2019MS001730>.
- Stensrud, D. J., 2007: *Parameterization Schemes*. Cambridge University Press, 449 pp.
- Stevens, B., C. H. Moeng, and P. P. Sullivan, 1999: Large-eddy simulations of radiatively driven convection: Sensitivities to the representation of small scales. *J. Atmos. Sci.*, **56**, 3963–3984, [https://doi.org/10.1175/1520-0469\(1999\)056<3963:LESORD>2.0.CO;2](https://doi.org/10.1175/1520-0469(1999)056<3963:LESORD>2.0.CO;2).
- Sun, J., S. P. Burns, A. C. Delany, S. P. Oncley, T. W. Horst, and D. H. Lenschow, 2003: Heat balance in the nocturnal boundary layer during CASES-99. *J. Appl. Meteor.*, **42**, 1649–1666, [https://doi.org/10.1175/1520-0450\(2003\)042<1649:HBITNB>2.0.CO;2](https://doi.org/10.1175/1520-0450(2003)042<1649:HBITNB>2.0.CO;2).
- Trapp, R. J., and Coauthors, 2020: Multiple-platform and multiple-Doppler radar observations of a supercell thunderstorm in South America during RELAMPAGO. *Mon. Wea. Rev.*, **148**, 3225–3241, <https://doi.org/10.1175/MWR-D-20-0125.1>.
- Trier, S. B., G. S. Romine, D. A. Ahijevych, R. J. Trapp, R. S. Schumacher, M. C. Coniglio, and D. J. Stensrud, 2015: Mesoscale thermodynamic influences on convection initiation near a surface dryline in a convection-permitting ensemble. *Mon. Wea. Rev.*, **143**, 3726–3753, <https://doi.org/10.1175/MWR-D-15-0133.1>.
- UCAR/NCAR, 1990: NCAR Integrated Surface Flux System (ISFS). Accessed 15 December 2020, <https://doi.org/10.5065/D6ZC80XJ>.
- , 2020: Multi-network composite highest resolution radiosonde data, version 1.3. UCAR/NCAR Earth Observing Laboratory, accessed 12 December 2020, <https://doi.org/10.26023/GKFF-YNBJ-BV14>.
- Varble, A., H. Morrison, and E. Zipser, 2020: Effects of under-resolved convective dynamics on the evolution of a squall line. *Mon. Wea. Rev.*, **148**, 289–311, <https://doi.org/10.1175/MWR-D-19-0187.1>.
- Vera, C., and Coauthors, 2006: The South American Low-Level Jet Experiment. *Bull. Amer. Meteor. Soc.*, **87**, 63–78, <https://doi.org/10.1175/BAMS-87-1-63>.
- Virtanen, P., and Coauthors, 2020: SciPy 1.0: Fundamental algorithms for scientific computing in Python. *Nat. Methods*, **17**, 261–272, <https://doi.org/10.1038/s41592-019-0686-2>.
- Wang, Q., M. Xue, and Z. Tan, 2016: Convective initiation by topographically induced convergence forcing over the Dabie Mountains on 24 June 2010. *Adv. Atmos. Sci.*, **33**, 1120–1136, <https://doi.org/10.1007/s00376-016-6024-z>.
- Weckwerth, T. M., J. W. Wilson, and R. M. Wakimoto, 1996: Thermodynamic variability within the convective boundary layer due to horizontal convective rolls. *Mon. Wea. Rev.*, **124**, 769–784, [https://doi.org/10.1175/1520-0493\(1996\)124<0769:TVWTCB>2.0.CO;2](https://doi.org/10.1175/1520-0493(1996)124<0769:TVWTCB>2.0.CO;2).
- , H. V. Murphey, C. Flamant, J. Goldstein, and C. R. Pettet, 2008: An observational study of convection initiation on 12 June 2002 during IHOP_2002. *Mon. Wea. Rev.*, **136**, 2283–2304, <https://doi.org/10.1175/2007MWR2128.1>.
- , J. W. Wilson, M. Hagen, T. J. Emerson, J. O. Pinto, D. L. Rife, and L. Grebe, 2011: Radar climatology of the COPS region. *Quart. J. Roy. Meteor. Soc.*, **137**, 31–41, <https://doi.org/10.1002/qj.747>.

- Weisman, M. L., 1992: The role of convectively generated rear-inflow jets in the evolution of long-lived mesoconvective systems. *J. Atmos. Sci.*, **49**, 1826–1847, [https://doi.org/10.1175/1520-0469\(1992\)049<1826:TROCGR>2.0.CO;2](https://doi.org/10.1175/1520-0469(1992)049<1826:TROCGR>2.0.CO;2).
- Wulfmeyer, V., and Coauthors, 2011: The Convective and Orographically-induced Precipitation Study (COPS): The scientific strategy, the field phase, and research highlights. *Quart. J. Roy. Meteor. Soc.*, **137**, 3–30, <https://doi.org/10.1002/qj.752>.
- Zipser, E. J., D. J. Cecil, C. Liu, S. W. Nesbitt, and D. P. Yorty, 2006: Where are the most intense thunderstorms on Earth? *Bull. Amer. Meteor. Soc.*, **87**, 1057–1072, <https://doi.org/10.1175/BAMS-87-8-1057>.